An Interdisciplinary Investigation of Conformational Changes in Quasi-Crystalline Protein Array R-bodies in Response to pH

Guangyang Cai

A dissertation

submitted in partial fulfillment of the

requirements for the degree of

Doctor of Philosophy

University of Washington

2023

Reading Committee:

Justin M. Kollman, Chair

Charles A. Asbury, Co-Chair

Alexey J. Merz

Program Authorized to Offer Degree:

Biochemistry

University of Washington

Abstract

An Interdisciplinary Investigation of Conformational Changes in Quasi-Crystalline Protein Array R-bodies in Response to pH

Guangyang Cai

Chair of the Supervisory Committee:

Justin M. Kollman

Biochemistry

R-bodies are ribbon-like protein polymers that undergo a dramatic conformational change from a tightly coiled form at neutral pH to an extended helical spiral at acidic pH. R-bodies were found in bacterial endosymbionts of paramecia, where their forceful extension causes vacuolar membranes to rupture contributing to a type of inter-paramecium warfare (Pond et al., 1989). Previous work has shown that R-body extension is fast, reversible, extremely robust, and tunable by directed evolution (Polka & Silver, 2016). However, it remains unknown how micron-scale changes in the conformation of an R-body ribbon arise from pH-induced changes in its nanoscale subunits. Here we use an interdisciplinary approach combining DIC microscopy, cryo-electron microscopy, atomic force microscopy, and hydrogen deuterium exchange to study individual, purified R-bodies *in vitro*. We show that R-body extension and contraction are highly cooperative and hysteretic processes with changes in the magnitude and direction of ribbon curvature as well as changes in ribbon thickness. Viewed *en face*, the R-body ribbon is a two-dimensional quasi-crystalline lattice with very small unit-cell dimensions (11.5 x 14.3 Å) that do not change with pH. Viewed edge-on, the ribbon has a laminar structure with five layers at

neutral pH, two of which become indistinct at acidic pH. We show that the C-termini of the main constituent helical proteins, Reb A and Reb B, undergo large pH-dependent changes in accessibility for hydrogen-deuterium exchange, implying a transition from disordered at neutral pH to ordered helices at acidic pH. We propose this disordered-to-helical transition in the C-termini of Reb A and Reb B alters the tension within the concave side of the ribbon, driving changes in the local curvature of the ribbon to cause the extension process. Our findings provide a basis for understanding the mechanism of R-body extension, which may guide efforts to engineer R-bodies for novel drug delivery applications or to design new dynamic protein arrays.

Acknowledgements

First, I want to thank my collaborators who supplied critical data for my thesis project. I want to thank Shuai Zhang for contributing the AFM data on whole R-bodies and fragmented R-bodies. Thank you, Kelli Hvorecny, for contributing the calculations for the R-body lattice parameters. And finally, thanks to Clint Vorauer and Mike Guttman for the HDX work.

Secondly, I would like to reflect on some of the challenges I have faced during my doctoral work at the University of Washington. In 2017, shortly after we had moved to Washington from California, my wife was diagnosed with Stage IIIB breast cancer and had to begin intensive treatment at the Seattle Cancer Care Alliance (now the Fred Hutch Cancer Center). We had no real connections in Washington state, so I was my wife's sole caregiver. The stress of the situation, coupled with my own crippling major depression with generalized anxiety disorder, nearly drove me to give up on my doctoral work. I can confidently say that without the guidance from my co-mentors, Justin Kollman and Charles Asbury, I would not be writing this acknowledgement or this thesis. Throughout my time at the University of Washington, I have always been amazed at the quality of the community here as exemplified by my co-mentors and the labs which they lead; I've never met people who were more understanding and willing to work with me through difficult circumstances. Even when my wife's cancer returned as Stage IV metastatic in 2022, it was the mentorship and encouragement from Justin and Chip which helped convince me to try to finish strong and finish my contribution to scientific research. In addition to the support from Justin and Chip, I want to especially give thanks to Erin Kirschner as my graduate school program coordinator. I've made it known to all potential applicants to the BPSD program that my trust in Erin was a key factor in deciding to come to the University of

Washington. Erin's confidence, compassion, and attention to detail has made juggling responsibilities between grad school, caregiver duties, and my own mental health as easy as it could be.

Finally, I want to thank my wife, Corey Brennan, for never giving up on me despite my own lack of self-confidence. Thank you for being patient with me; I know there's been a lot that's happened which changed our plans, but we've been able to remain flexible and optimistic despite the challenges put in our path.

Table of Contents

1. Introduction

Refractile Body (R-bodies) producing bacterial endosymbionts serve as membrane rupturing mechanisms in inter-paramecium competition.

Refractile bodies (R-bodies) are a group of large ribbon-like protein polymers that were originally discovered during studies of inter-paramecium competition between strains of "killer" and "sensitive" paramecium in the late 1930s (Sonneborn, 1938). These early studies noted that strains of "killer" paramecium would contain large "Kappa" particles in mostly the cytoplasm and occasionally the macronucleus. These Kappa particles were released into the growth medium when these killer paramecium strains were co-cultured with other competing paramecium strains (referred as "sensitive" strains). The sensitive strains would phagocytose the Kappa particles, which appeared to result in the killing of the sensitive strains over a time period of a few hours to several days. It was later found that these Kappa particles were actually R-body producing bacterial endosymbionts which would be shed by their killer paramecium host as a method of delivering toxins to kill sensitive paramecium strains (Preer, 1975). These R-body producing bacteria synthesize large, coiled R-body complexes as a mechanism to rupture the membrane of the phagocytic vacuole of the sensitive paramecium. The digestive environment of the phagocytic vacuole both breaks down the cell wall of the R-body bacterium and triggers the characteristic uncoiling of the R-body complex into a long helical rod in response to the acidification of the vacuole (Polka & Silver, 2016). The extension of the R-body complex physically ruptures and lyses both the bacterium and the digestive vacuole, resulting in spillage of digestive enzymes from the vacuole as well as any cytotoxic chemicals synthesized by the bacterium (Pond et al., 1989). Striking images of R-body containing bacteria and the phagocytic lysing process have been

captured by John R. Preer, Jr., Louise B. Preer, Artur Jurand, and Finn R. Pond, which can be seen in Figure 1.1 (Preer et al., 1974).

R-bodies can also be involved as part of host colonization mechanisms for *Pseudomonas aeruginosa.*

More recently, R-bodies have been shown to facilitate the opportunistic infection of diverse hosts such as plants and nematodes by pseudomonas. A Nature Communications article by Wang et al 2021 focused on the ability of *Pseudomonas aeruginosa* PA14 ability to infect *A. thaliana* and *C. elegans* contingent upon expression of a cluster of Reb genes which encode for PA14 R-body production. Wang et al demonstrated that stochastic expression of Reb genes and subsequent synthesis of PA14 R-bodies was necessary for full virulence in both plant host *A. thaliana* and animal host *C. elegans*. Specifically for *C. elegans*, Wang et al suggest that the phagolysosomal activity of PA 14 R-bodies may lead to translational inhibition in the nematode host cells by cleavage of ribosomes by uncontained phagosome contents and subsequent triggering of the *zip-2* pathway (B. Wang et al., 2021). This study highlights the role of R-body synthesis in diverse niches outside of their canonical role in inter-paramecium competition, and suggests re-examination of R-body production in other free living, non-endosymbiotic bacteria noted in prior studies of R-body producing bacteria (Pond et al., 1989). Moreover, the diversity of R-body representation may suggest a diversity of structures which accomplish similar membrane rupturing mechanisms.

Isolation of Type 51 R-body Reb locus plasmid in *Caedibacter taeniospiralis.*

One of the most extensively studied R-body producing bacterial endosymbionts is *Caedibacter taeniospiralis*, an endosymbiont of *Paramecium tetraurelia*. These bacteria are shed by their host killer strain paramecium to be phagocytosed by sensitive paramecia, where exposure to the acidic environment of the sensitive paramecium's digestive vacuole induces a dramatic conformational change in the R-body from a tight coil ~500 nm wide into a helical spiral ~10-20 μm long. The synthesis of R-bodies by *C. taeniospiralis* was suggested to be a trait inherited through exchange of an extrachromosomal element which was originally named "Kappa" (which resulted in the Kappa particle nomenclature), which allowed for both the transient and stochastic expression of R-bodies in a population of *C. taeniospiralis*. The extrachromosomal "Kappa" factor was later determined to be an R-body encoding locus on plasmid DNA in 1983 by Robert L. Quackenbush (Quackenbush, 1983), who demonstrated that the R-body encoding portion of the *C. taeniospiralis* plasmid could be cloned to reproduce R-body expression in *E. coli* (Kanabrocki et al., 1986). Subsequent cloning efforts identified the sequences of the specific Reb genes comprising the R-body locus (Jeblick & Kusch, 2005), which has allowed the development of recombinant R-body expressing plasmids for purification and testing of R-bodies in vitro (Fig 1.2A).

Structural and Biophysical in vitro studies on R-bodies purified from recombinant *E. coli.*

Initial in vitro studies of Type 51 R-bodies (hereto referred to as just R-bodies) purified from recombinant E. coli focused revealed numerous astonishing structural and biophysical properties of the R-body complex. First, R-bodies are incredibly structurally robust protein arrays. In a study by Kanabrocki et al, R-bodies purified from either *C. taeniospiralis* or recombinant *E. coli* were subjected to a rigorous gambit of protein dissociating conditions (Kanabrocki et al., 1986). A quote

from one of the study's co-authors, Finn R. Pond, best highlights the incredible toughness of R-bodies under grueling buffer conditions (perhaps to the mild annoyance of the inquisitive biochemist who seeks to understand the R-body's composition):

"Treatments included incubation in combinations of 8 M urea, 1 to 10%c SDS, and up to 5% 2-mercaptoethanol or dithiothreitol. Incubations were carried out at 100°C for up to 1 h. Additionally, incubation at 37°C for 2 h in 8.6 M guanidine hydrochloride or 6 M guanidine thiocyanate, followed by dialysis and standard treatment with the final denaturing and reducing sample buffer, did not result in greater R-body dissociation. Also, boiling the R bodies for 5 min in dilute hydrochloric acid (pH 1.8) had no noticeable effect on dissociation." (Pond et al., 1989)

The extreme toughness of R-bodies is reflected in the composition of the constitutive Reb elements as revealed by denaturing SDS-PAGE. Purified WT R-body samples demonstrate a consistent, reproducible pattern of protein bands across a much wider range of molecular weights than would be expected from the predicted molecular weight of any single Reb monomer (Fig.). This demonstrates that Reb proteins in the R-body complex must be extensively cross-linked with non-disulfide inter-peptide bonds. Anti-His tag Western blotting on His-tagged Reb proteins indicates that much of the R-body structure appears to contain extensively cross-linked Reb A and Reb B with small amounts of Reb D. However, all Reb proteins are necessary for full expression of R-bodies; the role of Reb C is still not yet known but is hypothesized to be catalytic or potentially an intermediate scaffolding protein which is not incorporated into the final R-body complex (Fig 1.2 B, C).

Aside from their robustness, R-bodies possess unique biophysical properties depending on their pH-dependent conformation. In neutral or basic pH, coiled R-bodies appear to settle out of solution to form a white, almost salt-like layer on the bottom of any container. In acidic pH, extended R-bodies remain suspended in solution as a cloudy, somewhat translucent mixture. In either conformation, R-body complexes can be pelleted from solution by a relatively low-speed centrifugation (between 5,000 to 10,000 x g) for less than 10 minutes. Another interesting property of R-bodies is their ability to interact with visible light. For example, their ability to refract light near 600 nm appears to depend on the conformation of the R-body where coiled form R-bodies appear to have higher absorbance at 600 nm wavelength than extended form R-bodies.

The unique biophysical properties of the two pH-dependent R-body conformations can be used in experiments which investigate the pH-controlled conformational change from coiled to extended form. Of particular note, an investigation of the pH-dependent conformational change in Polka & Silver 2016 took advantage of the difference in 600 nm wavelength light absorbance between the contracted, coiled form and the extended, helical form to track a bulk sample of R-bodies through hundreds of cycles of pH-induced conformational change (Fig 1.2D). Astonishingly, the ability of R-bodies to undergo pH-induced conformational change not only appears to be reversible, but also extremely reproducible with little (if any) loss of function over hundreds of cycles. These structural transitions are hypothesized to generate large forces given their in vivo role in membrane disruption; thus, it is reasonable to assume that the force generation potential of R-bodies also stays consistent over many cycles of conformational change. Furthermore, Polka and Silver were able to develop a plate-reader based assay to screen large numbers of point mutation R-body constructs by taking advantage of the coiled R-body pelleting and light absorbance characteristics. The results

of this assay demonstrate that even single point mutations in Reb A can dramatically alter the pH response of R-body complexes.

Interestingly, it has been demonstrated that R-body complexes purified from E. coli are not sufficient to kill paramecium (Schrallhammer et al., 2012), suggesting that R-body complexes are not inherently cytotoxic but serve as part of a delivery mechanism for delivery of cytotoxins that are co-expressed in their native bacterial endosymbionts. The unique structural and biophysical properties of R-bodies may make them ideal model systems for designing force-generating protein machines, and as a platform for designing novel therapeutic or biosensor applications.

Interdisciplinary Thesis research on R-bodies

Currently, there are neither high-resolution molecular structures nor any proposed mechanical transition models for R-bodies. Determination of molecular structures of R-bodies in different buffering conditions and characterization of the kinetics of the conformational transition between buffering conditions would provide not only a greater understanding of the intrinsic relationship between R-body structure and function, but also a strong fundamental basis for the use of R-body structures in rational design of protein machines. Here, I use an interdisciplinary approach combining my work with DIC microscopy, negative stain electron microscopy, cryo-electron microscopy, cryo-electron tomography, and sub-tomogram averaging in collaboration with results from atomic force microscopy (performed by Shuai Zhang, Jim DeYoreo, and Jiajun Chen) and hydrogen deuterium exchange (performed by Clint Vorauer and Mike Guttman) to study individual, purified R-bodies *in vitro*. We discovered that R-body extension and contraction are highly cooperative and hysteretic processes, involving changes in the magnitude

and direction of ribbon curvature and changes in ribbon thickness, but not in ribbon length or width. Viewed en face, the R-body ribbon consists of a two-dimensional quasi-crystalline lattice, with very small unit-cell dimensions of 11.5 x 14.3 Å that do not change with pH. While the main constituent proteins, RebA and RebB, are predicted to be mostly α-helical, we show that their C-termini undergo large pH-dependent changes in accessibility for hydrogen-deuterium exchange, implying a transition from initially disordered at neutral pH to ordered, and probably α-helical at acidic pH. We propose that this disordered-to-helical transition in the C-termini of RebA and RebB alters the tension within one or two laminae on the concave side of the ribbon, thereby changing the local curvature of the ribbon and driving the extension process.

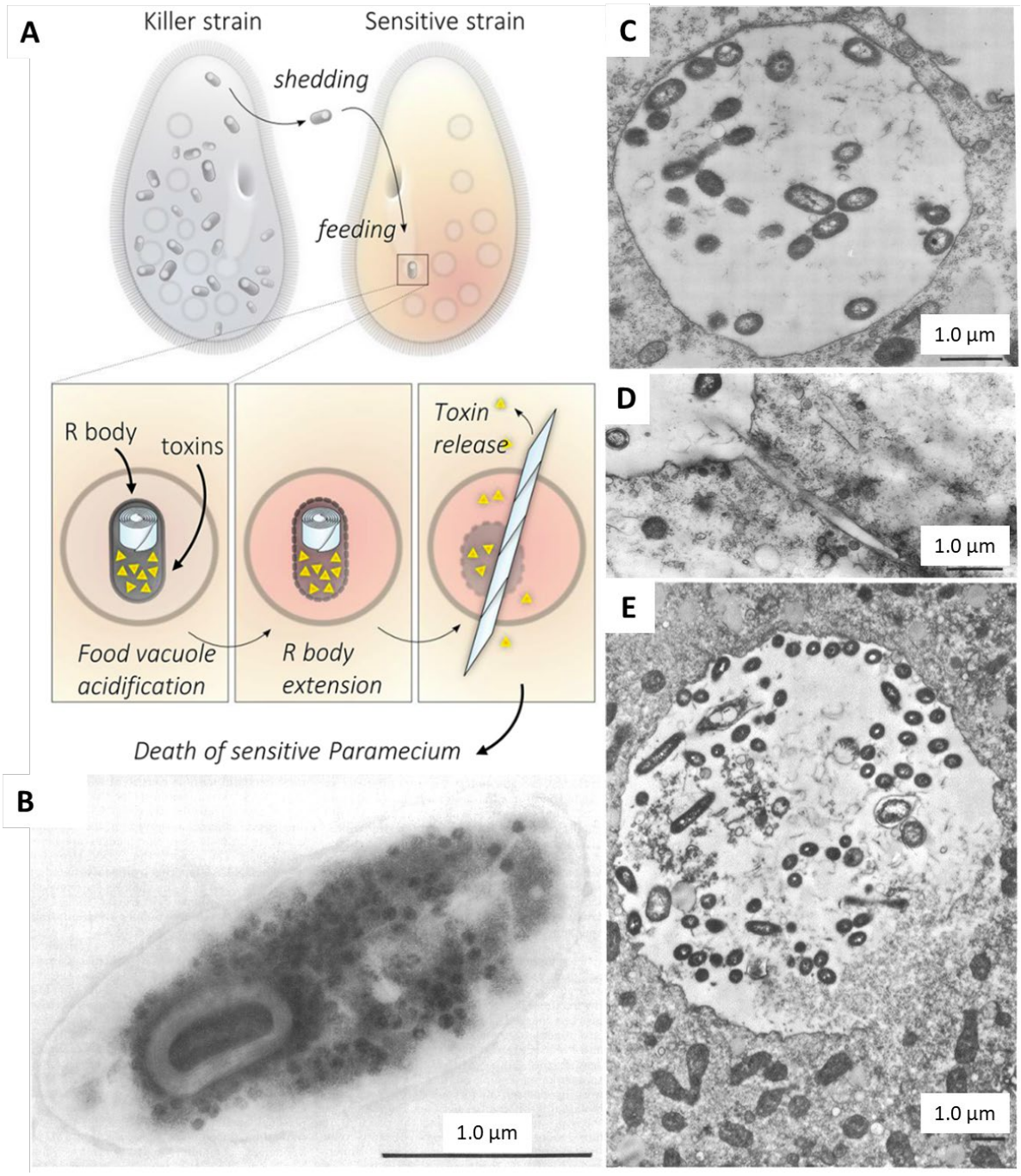

Figure 1.1: R-bodies are pH sensitive protein pistons employed for inter-paramecium competition.

A) Diagram of inter-paramecium competition between R-body hosting killer strains and the R-body sensitive strain (Polka & Silver, 2016). B) A section of bacterial endosymbiont *C. varicaedens* with white R-body and dark toxins (Pond et al., 1989). C) Paramecium food vacuole filled with dark R-body bacteria (Preer et al., 1974). D) Extended R-body puncturing vacuole membrane (Preer et al., 1974). E) Food vacuole ruptured by R-bodies extending out from the bottom right (Preer et al., 1974).

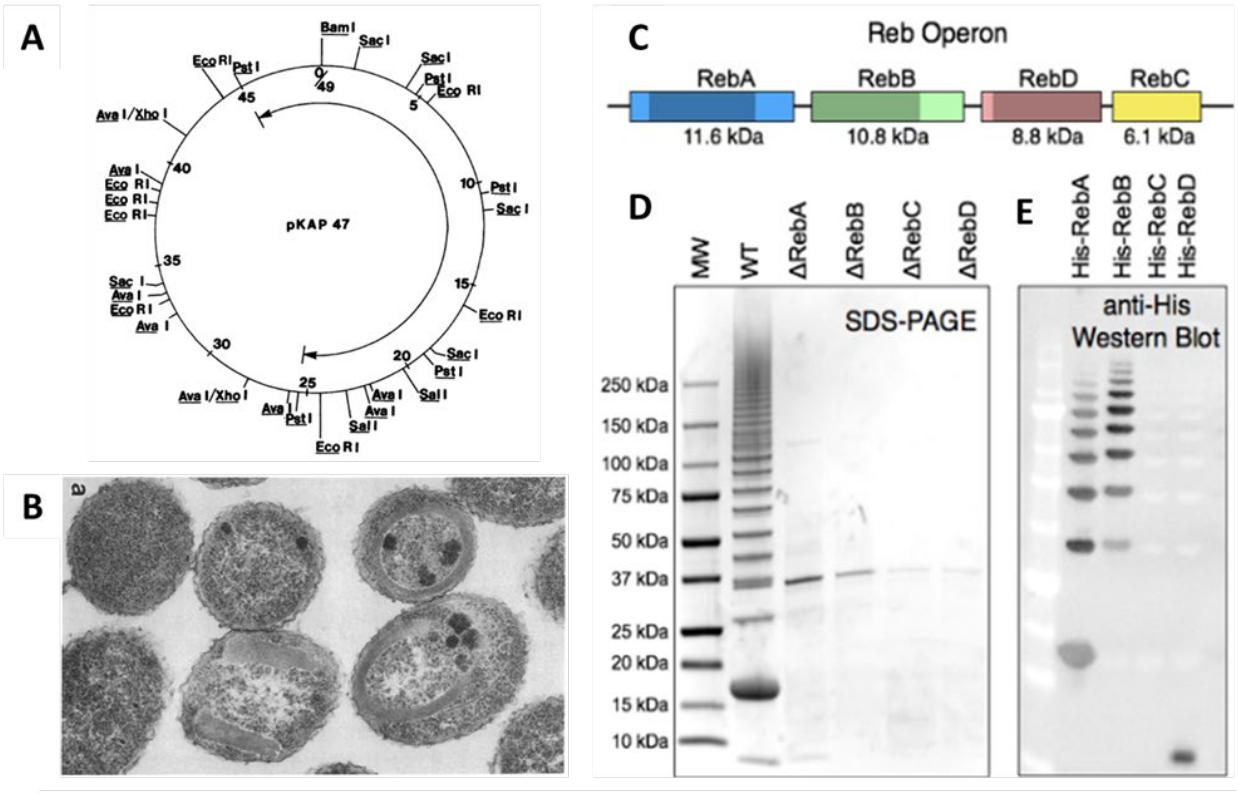
A
Bam I
Sac I
Sac I
Pst I
Eco RI
Eco RI
Pst I
Ava I/Xho I
Ava I
Eco RI
Eco RI
Eco RI
Sac I
Ava I
Eco RI
Ava I
Ava I/Xho I
Ava I
Pst I
Sal I
Ava I
Sal I
Pst I
Sac I
Eco RI
pKAP 47
0
5
10
15
20
25
30
35
40
45
49
B
C
Reb Operon
RebA
RebB
RebD
RebC
11.6 kDa
10.8 kDa
8.8 kDa
6.1 kDa
D
MW
WT
ΔRebA
ΔRebB
ΔRebC
ΔRebD
SDS-PAGE
250 kDa
150 kDa
100 kDa
75 kDa
50 kDa
37 kDa
25 kDa
20 kDa
15 kDa
10 kDa
E
His-RebA
His-RebB
His-RebC
His-RebD
anti-His
Western Blot

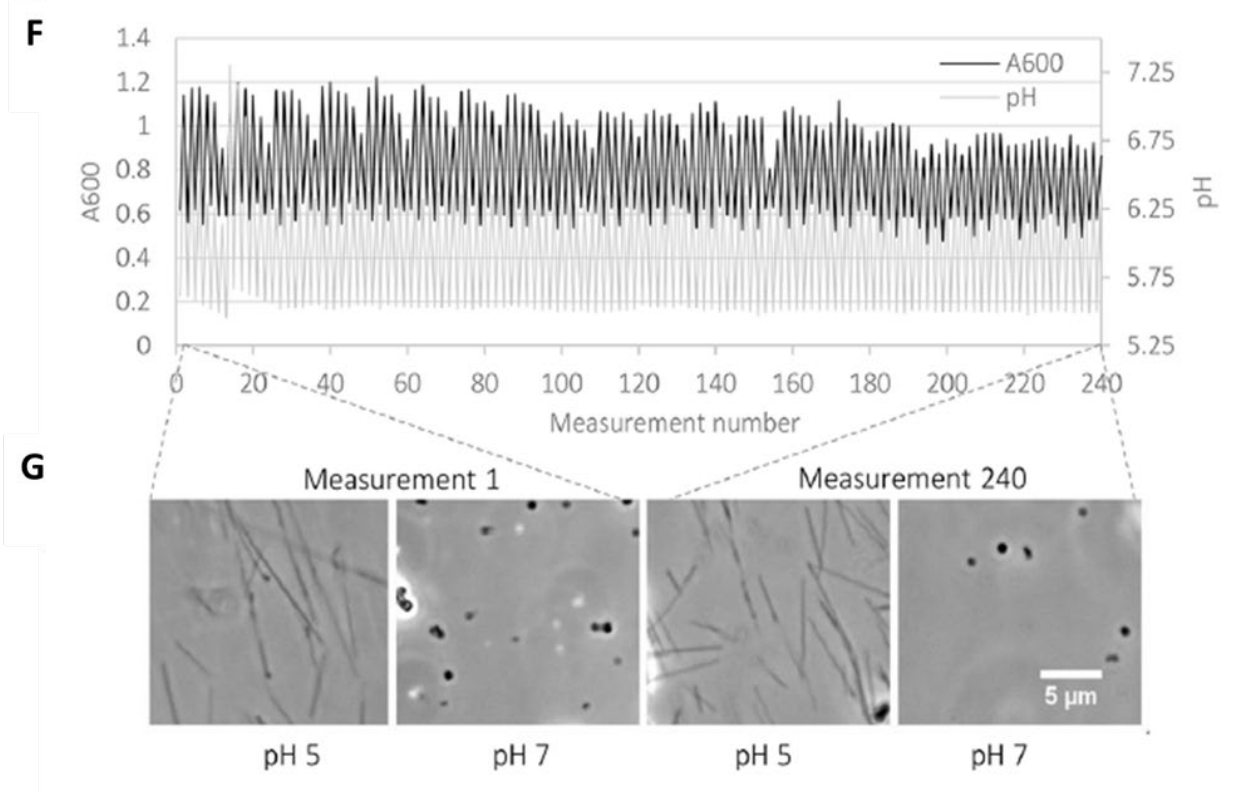
F
A600
pH
1.4
1.2
1
0.8
0.6
0.4
0.2
0
7.25
6.75
6.25
5.75
5.25
0
20
40
60
80
100
120
140
160
180
200
220
240
Measurement number
G
Measurement 1
Measurement 240
5 µm
pH 5
pH 7
pH 5
pH 7

Figure 1.2: Isolation of native R-body producing plasmids allows in vitro testing of R-body structure and function.

A) A diagram of a plasmid pKAP47 isolated from *C. taeniospiralis*; the arrow highlights the region which was transformed into E. coli (Quackenbush & Burbach, 1983). B) E. coli producing R-bodies after transformation with recombinant R-body plasmid (Quackenbush & Burbach, 1983). C) Diagram of operon of Reb proteins which polymerize into R-bodies (Kollman R-body grant). D) SDS-PAGE of WT R-bodies and different constructs with a single Reb protein knocked out. E) Western blot of full Reb constructs with His-tag on different Reb protein. (F) Bulk absorbance measurements of R-bodies undergoing hundreds of pH cycles (Polka & Silver, 2016). G) Images R-bodies from first and last cycles show no noticeable difference even after hundreds of conformational cycles.

Figure 1.3: Type 51 Reb sequences from *Caedibacter taeniospiralis*.

A) Amino acid sequences of Reb A, B, C, and D from *C. taeniospiralis*. B) Multiple sequence alignment of Reb A, B, and D to other Reb-like proteins from other bacteria.

2. Results

R-body extension and contraction are highly cooperative and hysteretic processes.

In response to changes in pH, R-bodies undergo reversible transitions between a tightly coiled and an extended helical form (Fig 2.1 A), but the kinetics of these transitions have not been described. To measure rates of extension and contraction, we imaged individual purified R-bodies by differential interference contrast (DIC) microscopy. The R-bodies were expressed recombinantly in *E. coli*, purified, and then attached sparsely to the glass wall of a flow channel, enabling single R-bodies to be viewed continuously while the buffer was exchanged between a neutral or basic pH and an acidic pH. When exchanged from pH 7 to pH 5, the R-bodies extended from their initially coiled state by many micrometers in a few seconds (Fig. 2.1 B, left). Upon exchange from pH 5 back to pH 7, the extended R-bodies rapidly contracted again into a compact form (Fig. 2.1 B, right). The transition behavior of single R-bodies was usually repeatable over many exchanges between pH 5 and pH 7, consistent with previous light-scatter measurements showing that suspensions of R-bodies can undergo hundreds of pH-induced transitions without much loss of activity (Polka & Silver, 2016). We recorded time-lapse movies of many transition events and manually measured the R-body lengths in selected frames of each movie. Plots of length versus time for individual R-bodies during extension and contraction were sigmoidal, with an initial acceleration phase, followed by a linear phase when the extension or contraction speed was roughly constant, and ending with a deceleration phase (Fig. 2.1 C).

To explore how extension and contraction speeds depend on pH, we recorded transitions across a wide pH range. Extensions were recorded by starting at pH 7 and then exchanging with different

buffers ranging from pH 4 to 6.5. Similarly, contractions were recorded by starting at pH 5 and then exchanging with buffers ranging from pH 6.5 to 8.4. Speeds for individual R-body transitions were quantified by plotting length versus time and fitting the central, linear phase of the curve (Fig. 2.1 C). Contraction speeds increased with increasing pH, up to a maximum of 23 ± 0.7 $\mu m \cdot s^{-1}$ above pH 8 (Fig. 2.1 D) based on a sigmoidal fit to the average speeds. Conversely, extension speeds were highest at low pH, and they plateaued below pH 5.2 at only 7.0 ± 0.5 $\mu m \cdot s^{-1}$. We speculate that the lower maximal speed of extension compared to contraction may also suggest additional energetic barriers to the extension process which are not present in the contraction process; for example, there may be intra-ribbon interactions present in the coiled form which must be disrupted as part of the extension process, which would be expected to specifically slow extension without affecting contraction.

Within a narrow pH range, between pH 6.2 and 6.5, both the extension and contraction speeds were essentially zero (Fig. 2.1 D, gray shaded region). R-bodies that began in a tightly coiled form at pH 7 remained contracted after buffer exchange to pH 6.2 or pH 6.5, whereas R-bodies that began in an extended form at pH 5 remained extended after exchange into this same pH range. This history-dependent behavior is an example of surprisingly stable hysteresis: contracted R-bodies stored at pH 6.25 remained contracted for up to six days but were nevertheless capable of immediately extending upon buffer exchange to pH 5. Similarly, extended R-bodies stored at pH 6.25 remained extended for up to six days, but immediately contracted when exchanged to pH 7 (Fig. 2.2). The long-term stability of both extended and contracted forms within the hysteretic pH range indicates kinetic trapping and suggests a high degree of cooperativity between the subunits comprising an R-body ribbon, such that inter-

subunit contacts are energetically most favorable when neighboring subunits adopt the same configuration, either contracted or extended.

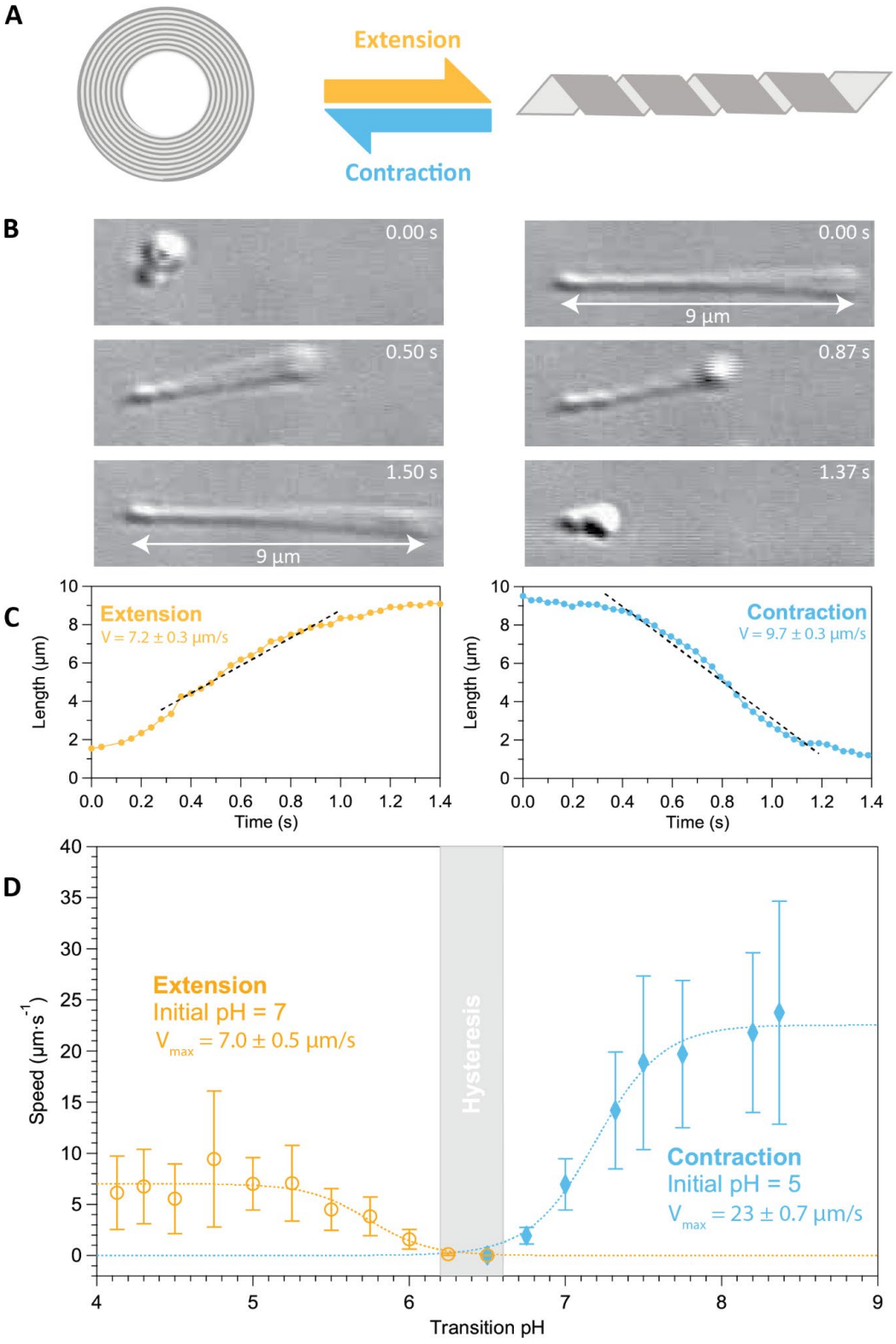
A
Extension
Contraction
B
0.00 s
0.50 s
1.50 s
9 µm
0.00 s
9 µm
0.87 s
1.37 s
C
Extension
V = 7.2 ± 0.3 µm/s
Length (µm)
Time (s)
Contraction
V = 9.7 ± 0.3 µm/s
Length (µm)
Time (s)
D
Extension
Initial pH = 7
V max = 7.0 ± 0.5 µm/s
Hysteresis
Contraction
Initial pH = 5
V max = 23 ± 0.7 µm/s
Speed (µm·s-1)
Transition pH

Figure 2.1: R-bodies undergo a reversible structural transition which is highly cooperative and hysteretic.

A) A diagram of the reversible pH-dependent conformational change experienced by R-bodies. B) Selected exemplary frames from DIC movies of individual R-body contracting (left) or extending (right) under buffer exchange to pH 7 or 5 respectively. C) Representative traces of individual R-body contracting (left) or extending (right) as tracked from DIC movies. The estimations of the extension and contraction speeds are calculated from a linear fit (black dashed line) to the middle of the transition. D) Quantification of extension and contraction speeds for R-bodies exchanged to different pH buffers. Points shown are mean +/- STD

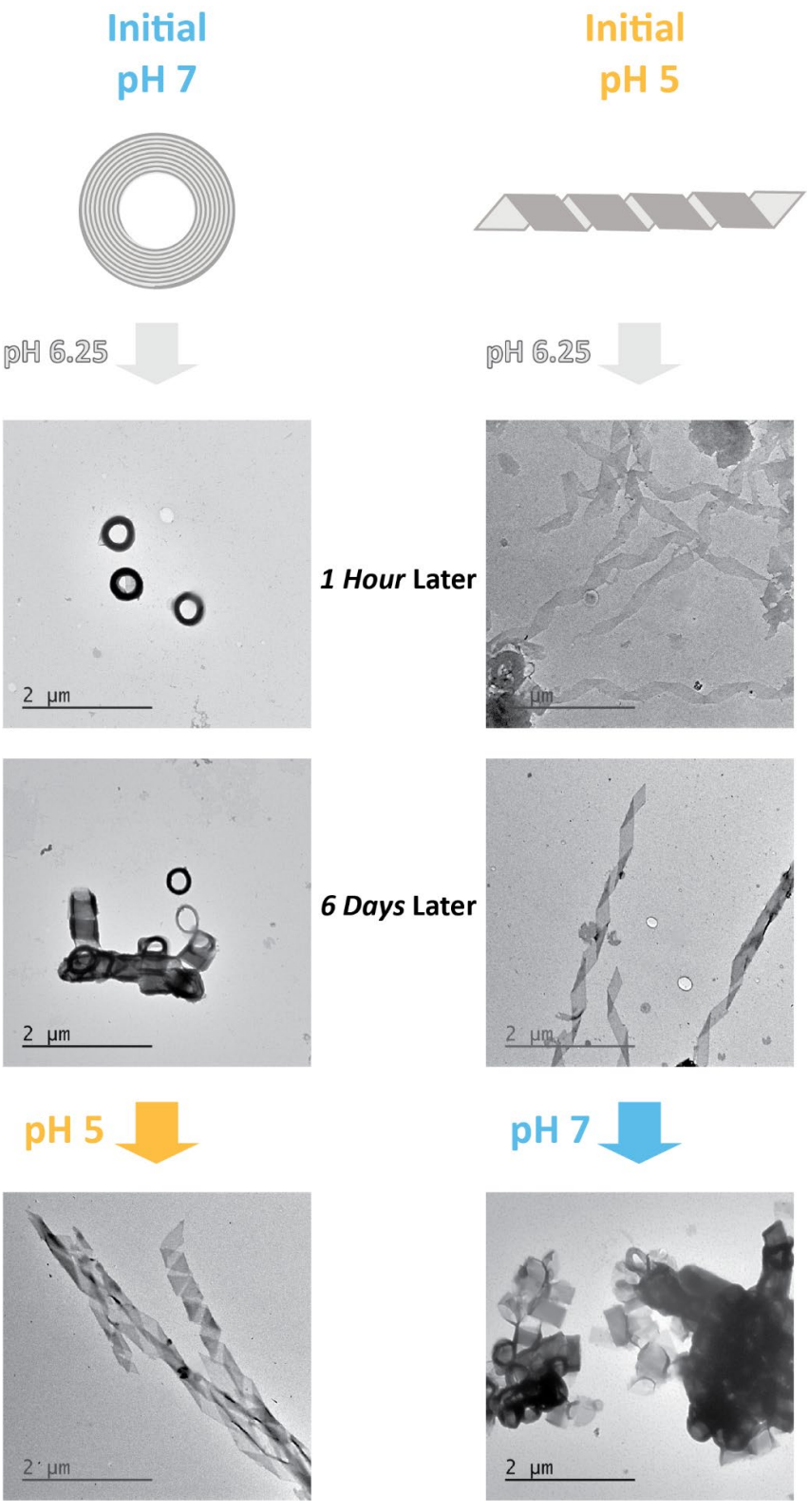
Initial
pH 7
Initial
pH 5
pH 6.25
pH 6.25
2 µm
1 Hour Later
µm
2 µm
6 Days Later
2 µm
pH 5
pH 7
2 µm
2 µm

Figure 2.2: The R-body structural transition is stably hysteretic.

R-bodies initially contracted at pH 7 or extended at pH 5 maintain their initial conformation when exchanged to the same pH 6.25 buffering conditions at RT. After 6 days at pH 6.25, R-bodies are still able to undergo the expected pH-induced conformational change in response to buffer exchange to the appropriate pH 5 or pH 7 buffer.

Macroscopic pH-induced changes in curvature across whole R-body complexes are consistent with local changes in the magnitude and direction of curvature radius in the constitutive R-body ribbon.

Observations of numerous individual R-bodies from DIC demonstrated that R-bodies can vary in the total length of the extended form. This variance in length and possibly other physical dimensions of both the coiled and extended states has yet to be systematically quantified. To quantify the various dimensions of the two R-body conformations, we performed cryo-electron tomography on R-body complexes in both coiled conformation at pH 7 and extended conformation at pH 5 to generate 3D volumetric tomograms of individual R-body complexes to take measurements of different R-body dimensions (Fig. 2.3). Our tomograms show R-bodies appear as ribbon-like structures with striking physical differences in curvature between extended pH 5 and contracted pH 7 conformations, and AFM of R-body complexes highlight the striking differences in surface curvature between the two conformations (Fig. 2.4 A, 2.4 B).

When transitioning from contracted form to extended form, the inner diameter of the R-body complex shrinks from an inner diameter, $\boldsymbol{d}$, of 318 ± 2.1 nm (N = 14) in the contracted form to an inner diameter, $\boldsymbol{c}$, of 118 ± 0.05 nm (N = 25) in the extended form (Fig. 2.4 C). This reduction in the inner diameter is consistent with the dramatic differences in curvature observed in extended R-bodies relative to contracted R-bodies by both cryo-tomography and AFM. Our measurements and calculations suggest that the total contour length, $\boldsymbol{S_c}$ vs $\boldsymbol{S_e}$, and width, $\boldsymbol{w_c}$ vs $\boldsymbol{w_e}$, of the R-body ribbon do not change between the contracted and extended conformations (Fig 2.3). This suggests that the molecular mass or composition of the R-body does not change between either conformation. Instead, the two distinct R-body conformations are due to a re-arrangement of the ribbon which comprises the R-body complex. The invariance of the contour length and width

may further support the hypothesis that small changes in the relative arrangement of an underlying subunit in the R-body ribbon may underlie the enormous macroscopic changes in structure observed between the contracted and extended conformations.

To investigate structural changes in curvature within the R-body ribbon, we mechanically sheared R-body complexes by high-pressure homogenization and imaged fragments by *in-situ* liquid AFM. This approach allows us to keep track of the same fragment of R-body ribbon through exchanges of different pH buffers to see what nanoscale structural changes may occur consistently through an R-body complex. From our *in-situ* AFM, we demonstrate that even when physically disrupted into sheared fragments, the R-body ribbon demonstrates obvious changes in both the magnitude of ribbon curvature **AND** the direction of the axis of curvature when tracked by in-situ AFM through multiple exchanges between high and low pH buffers (Fig. 2.4 D). This suggests that the dramatic macroscopic changes seen across R-body complexes are closely tied to consistent nanoscale structural changes in the R-body ribbon.

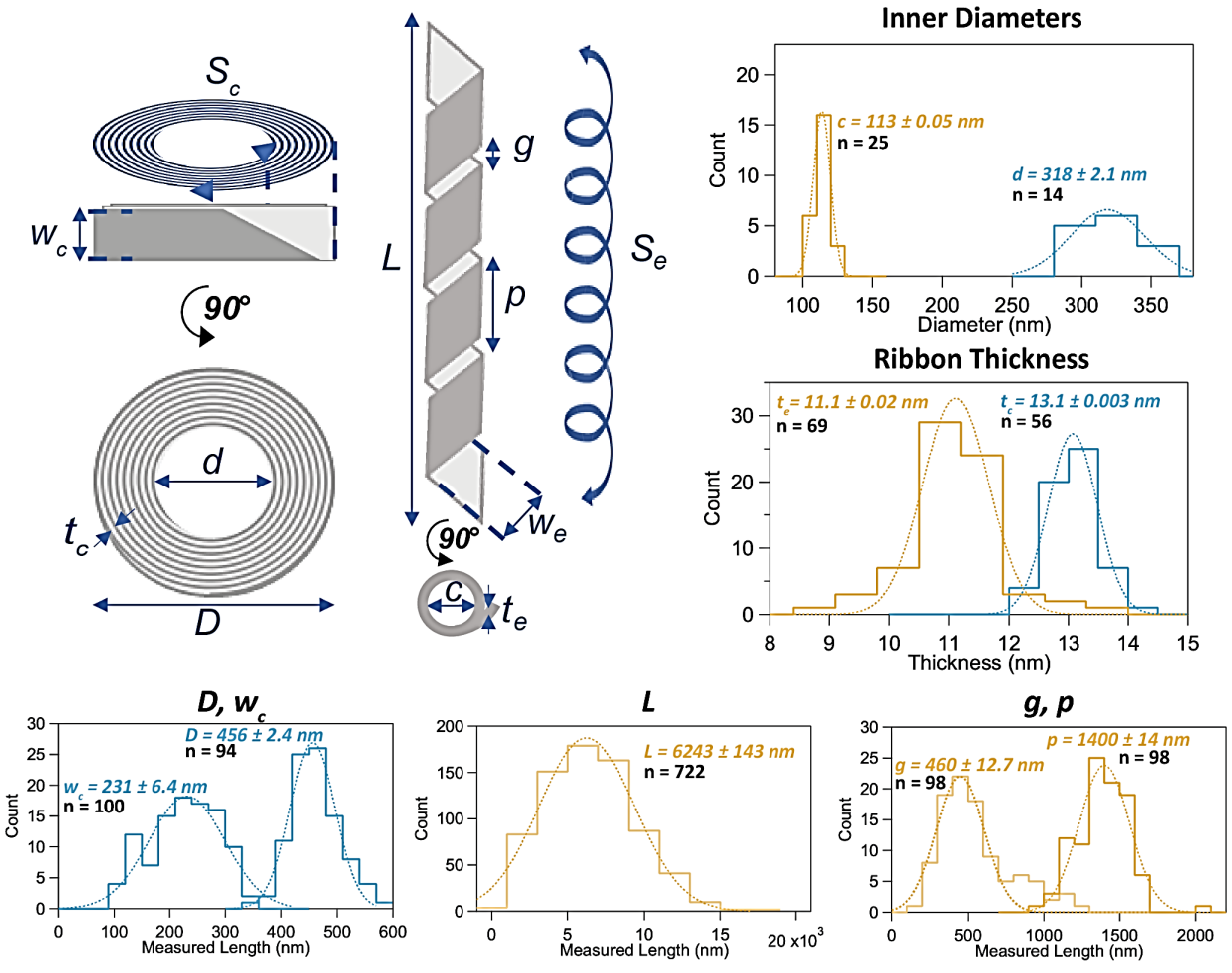

$$S_c = \frac{\pi(D^2 - d^2)}{4t_c} = 6288 \pm 149\ nm \qquad S_e = \frac{L}{p}\sqrt{(\pi c)^2 + p^2} = 6443 \pm 148\ nm$$

$$w_e = (p - g)\sin\left(\arctan\left(\frac{\pi c}{p}\right)\right) = 232 \pm 3\ nm$$

Figure 2.3: R-body ribbon length and width appear invariant between contracted and extended conformations.

Diagrams of contracted and extended R-body conformations labeled with different structural parameters, distributions measured for each labeled structural parameter, and equations to calculate values for parameters S_c, S_e, and w_e. S_c is an equation for the length of a coiled sheet. S_e is an equation for the length of a helical bar. W_e is derived in supplementary figure 3. Calculated values are shown with the propagation of uncertainty calculated using https://uncertaintycalculator.com/.

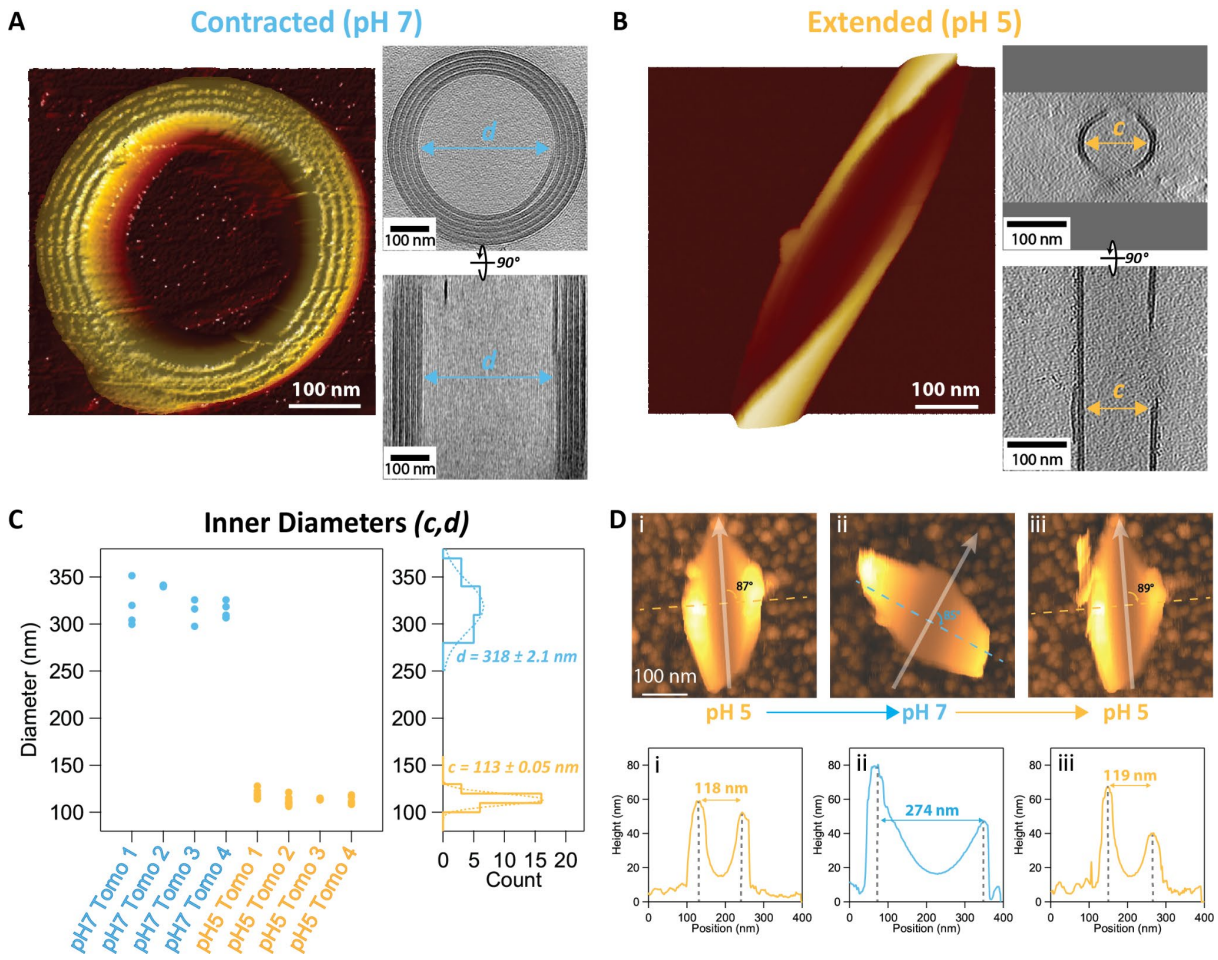

Figure 2.4: Macroscopic changes in curvature between high and low pH R-body conformations are consistent with local changes in magnitude and direction of curvature radius in the constitutive R-body ribbon.

A) R-body complex in contracted conformation at pH 7 visualized by AFM (left) and corresponding slices of tomograms low-pass filtered to 50Å (right) labeled with the contracted inner diameter measurement, ***d***. B) R-body complex in extended conformation at pH 5 visualized by AFM (left) and corresponding slices of tomograms low-pass filtered to 50Å (right) labeled with the extended inner diameter measurement, ***c***. C) Measurements of the inner diameters ***d*** vs ***c*** for R-bodies in contracted and extended conformation. Histograms and fits for each type of measurement is shown to the right with average values indicated (***d*** = 318 nm, ***c*** = 113 nm). D) In-situ AFM images in height mode tracking the same R-body fragment during multiple changes in pH buffer conditions (top) and the respective line scans of curvature across the dashed lines (bottom).

Assumption: In its extended form, the ribbon's outer face falls entirely on the surface of an imaginary cylinder, whose diameter is given by c. The edges of the ribbon will follow two helices of identical pitch, p, that also fall on the same cylinder's surface.

If this imaginary cylinder were split open and laid flat, it would look like the diagram below, where α represents the angle between the helical edges and the long-axis of the cylinder.

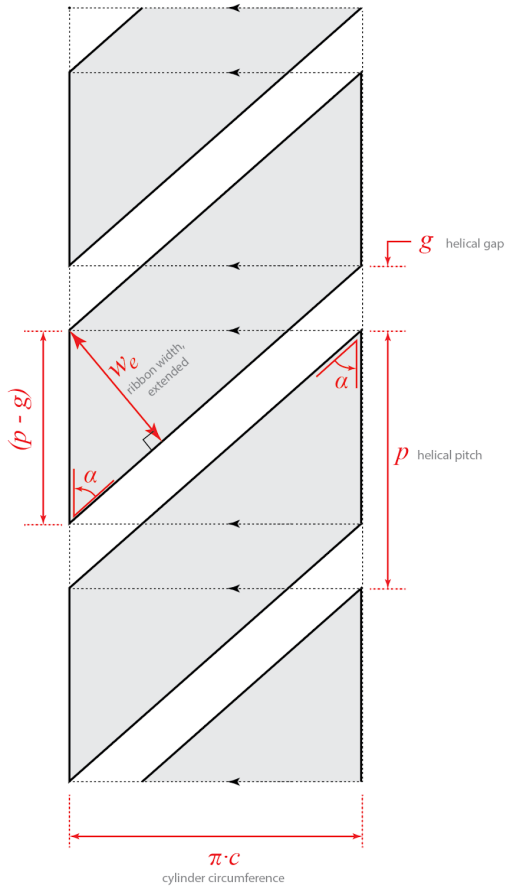

$$tan(\alpha) = \frac{\pi \cdot c}{p}$$

therefore,

$$\alpha = arctan\left(\frac{\pi \cdot c}{p}\right) \quad \text{eqn A}$$

$$sin(\alpha) = \frac{w_e}{(p - g)}$$

therefore,

$$w_e = (p - g) \cdot sin(\alpha) \quad \text{eqn B}$$

Substitute equation A (α) into equation B:

$$w_e = (p - g)\sin\left(\arctan\left(\frac{\pi c}{p}\right)\right)$$

Figure 2.5: Derivation of formula for w_e

The R-body ribbon changes both thickness and surface order in response to pH, with a clear lattice at low pH and no observable lattice at high pH

Of the many physical dimensions quantified for both extended and contracted conformations, there appeared a consistent and obvious change in the thickness of the R-body ribbon in response to changes in pH. The thickness of the R-body ribbon was measured by averaging tomographic slices through Z at different depths down the R-body central axis in both high pH and low pH. These averaged slices were used to generate 1D profiles across the R-body ribbon orthogonally to the ribbon face, and thickness values were estimated by calculating the distance between the half-max values at the opposite sides of the ribbon.

In the contracted conformation at high pH, the contracted R-body ribbon appears to have a thickness, t_c, of 13.1 ± 0.003 nm (Fig. 2.6 A, 2.6 B). In the extended conformation at low pH, the ribbon thickness, t_e, appears more compressed to a value of 11.1 ± 0.02 nm (Fig. 2.6 A, 2.6 B) Notably, the decrease in thickness from contracted to extended form corresponds to a decrease in the number of distinct layers within the R-body ribbon transitioning from pH 7 to pH 5, which further reinforces that critical structural changes are occurring within the R-body ribbon. As with the changes in curvature, we wanted to determine if changes in thickness would be reproduced in the R-body ribbon after mechanical disruption of the R-body complex. To achieve this, various R-body fragments were visualized by AFM at both pH 7 and pH 5 on mica. Consistent with our measured thickness difference, R-body fragments at pH 7 had larger height values relative to R-body fragments at pH 5 (Fig 2.6 C, 2.6 D).

Unexpectedly, AFM surface scans showed a difference in ribbon surface order dependent on pH. At pH 5, there appeared to be a definite lattice to the inner curved surface of R-body fragments

(Fig 2.6 E, 2.6 F). However, there did not appear to be any such lattice at pH 7, and the surface appeared amorphous. These data suggested the surface of the R-body ribbon changes from a disordered state at high pH to an ordered lattice at low pH, which suggests that changes in ribbon thickness are tied to a restructuring of the ribbon surface in response to pH. To confirm the presence of a lattice like surface, R-body fragments were imaged by cryo-electron microscopy as we expect the R-body ribbon to be highly ordered at least at low pH like a 2D protein array. The Fourier space of well-ordered 2D arrays demonstrate discrete reflections analogous to the diffraction spots seen in X-ray crystallography. Surprisingly, a careful analysis of both high and low pH R-body fragments by Kelli Hvorecny of the Kollman Lab demonstrates identical distinct reflections in Fourier space. This suggests that at least some portion of the R-body ribbon must be consistently ordered between both high and low pH, and that this order may only persist in a discrete sub-layer of the R-body ribbon as a shared stable lattice layer at both pH states (Fig. 2.7 A).

Observations from partially sheared R-body fragments in AFM helped to confirm the presence of a shared stable lattice. We interpret these partially sheared R-body fragments as a sub-population of fragments which have been partially stripped of a sub-layer of the R-body ribbon instead of being cleanly broken up with all layers intact (Fig. 2.7 B, 2.7 C). These partially sheared R-body fragments show the presence of two distinct layers within the R-body ribbon which respond differently to changes in pH. Notably, there appears to be a layer which changes from a disordered state at high pH to an ordered lattice at low pH (“top layer”) and a layer which remains a stable lattice at both high and low pH (“bottom layer”) (Fig 2.7 D, 2.7 E). This suggests that the R-body ribbon behaves as a biphasic material with a stable “bottom layer” lattice constant at all pH and a dynamic “top layer” which forms its own lattice at acidic pH but

loses order at neutral to basic pH. Moreover, the biphasic nature of the R-body ribbon suggests some systematic arrangement of constitutive Reb proteins to form distinct sub-layers with such different properties.

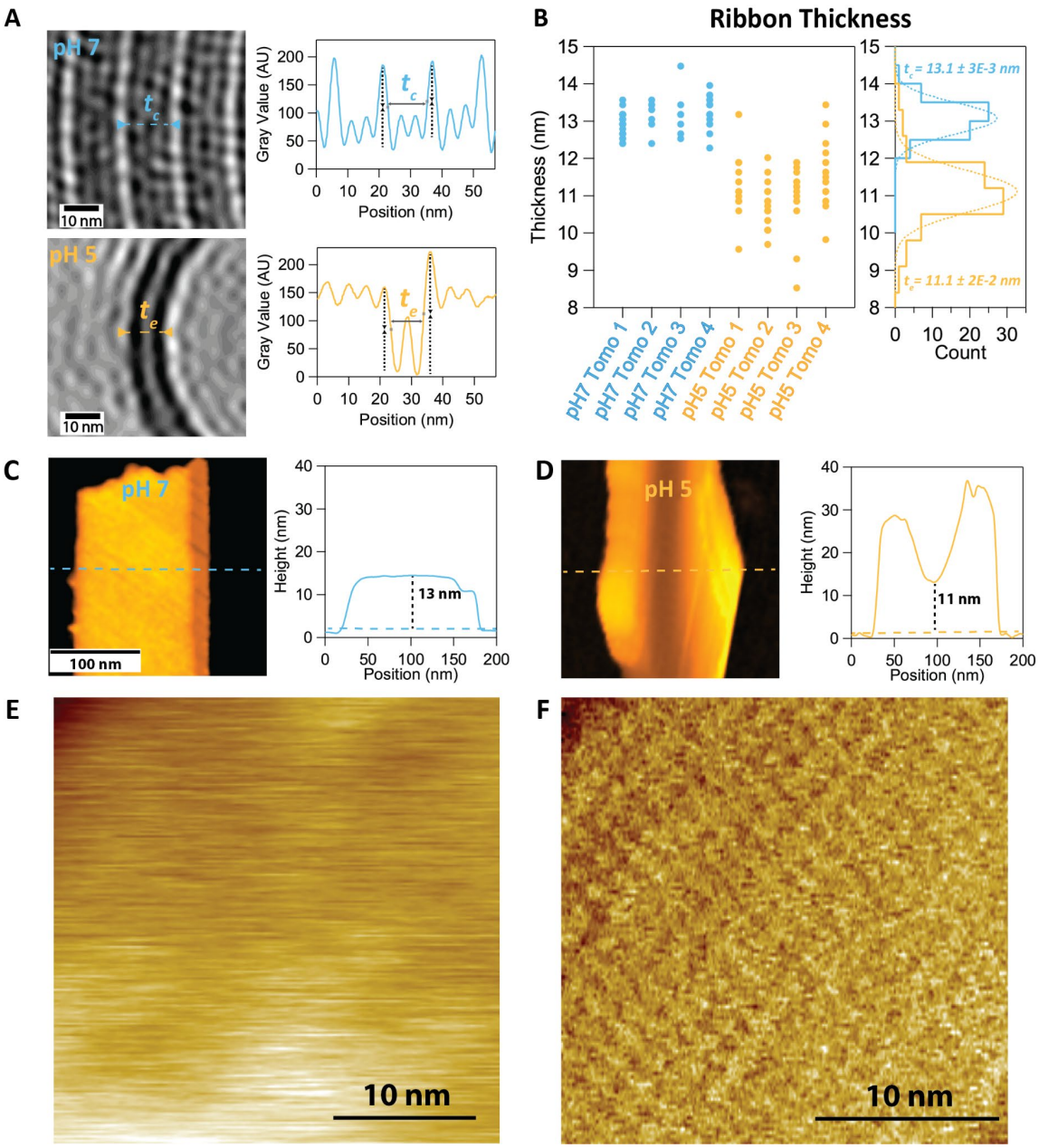

Figure 2.6: pH changes cause changes in R-body ribbon thickness, which appears to correlate to changes in surface order.

A) (Top) Projection through tomogram slices of pH 7 contracted R-body ribbon (left) and line scan (right) of the dashed lines using half-max gray value to measure ribbon thickness, t_c. (Bottom) Projection through tomogram slices of pH 5 contracted R-body ribbon (left) and line scan (right) of the dashed lines using half-max gray value to measure ribbon thickness, t_e. B) Measurements of the ribbon thickness for R-bodies in contracted and extended conformation. Histograms and fits for each type of measurement is shown to the right with average values

indicated (t_c = 13.1 nm, t_e = 11.1 nm). C) Exemplar AFM image of a pH 7 R-body fragment at 13 nm height. D) Exemplar AFM image of a pH 5 fragment at 11 nm height. E) Exemplar AFM image of a pH 7 fragment surface showing no ordered surface lattice. F) Exemplar AFM image of a pH5 fragment showing an ordered surface lattice.

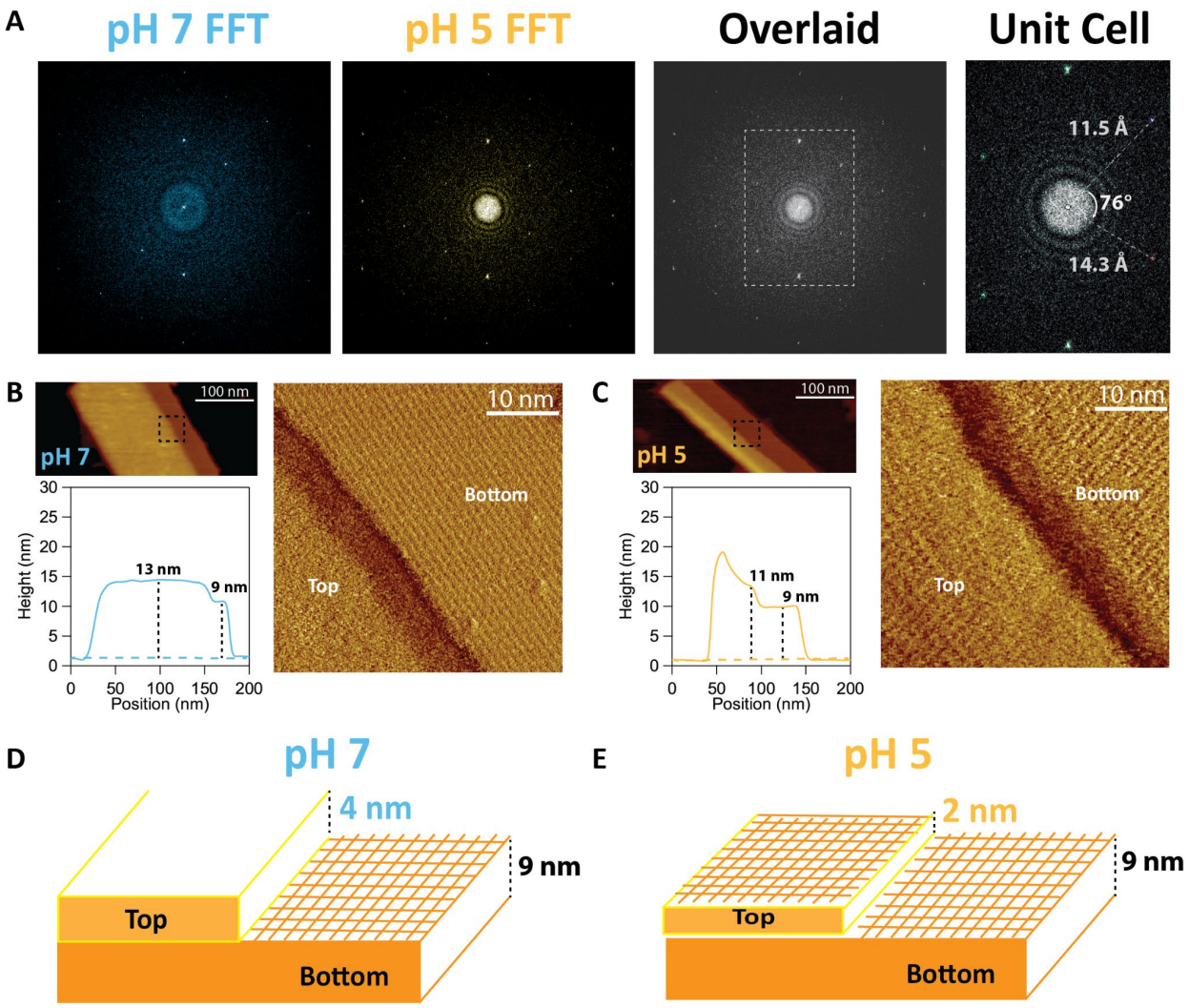

Figure 2.7: C-terminal regions of Reb A and Reb B proteins in the R-body ribbon drive the pH responsive conformational change.

A) Fourier reflections of cryo-TEM images of R-body fragments showing a shared stable lattice between pH 7 and pH 5 buffered R-body ribbon fragments. The unit cell of the shared lattice is very small, measuring at 11.5 Å by 14.3 Å with an angle of 76°. B) An exemplar partially sheared R-body fragment (left, top) with the corresponding line scan of height (left, bottom). The top layer of these partially sheared fragments does not show a clear lattice while the bottom layer is a clear lattice (right). C) An exemplar partially sheared R-body fragment (left, top) with the corresponding line scan of height (left, bottom). Images of partially sheared R-body fragments at pH 5 demonstrate lattices in both top and bottom layers. D) Diagram of partially sheared pH 7 fragment. E) Diagram of partially shared pH 5 fragment showing a top lattice on top of the stable lattice shared with pH 7 state.

The C-terminal regions of Reb A and Reb B proteins in the R-body ribbon are essential to driving the pH-responsive structural transition of R-body complexes.

Production of R-body complexes depends on the presence of all four proteins (Reb A, B, C, and D) in the Reb locus. Of these small Reb proteins, only Reb A, B, and D appear to be incorporated into the fully formed R-body complex with extensive cross-linking of Reb A and Reb B. All three incorporated Reb proteins share a "Reb" domain which is strongly predicted to be α-helical in its secondary structure by PsiPRED. However, Reb A and B have additional C-terminal regions outside of the Reb domain which are predicted to be weakly α-helical (Fig. 2.8 A). The role of this weakly structured C-terminal region of Reb A and Reb B is suggested to be important to the pH responsive transition (Polka & Silver, 2016), and changes in structure in this region should have important consequences for overall R-body structure. We performed hydrogen-deuterium exchange (HDX) experiments of R-bodies at high and low pH to investigate if there were any obvious changes in secondary structure between the contracted and extended conformations.

Strikingly, the HDX profiles of Reb A and Reb B demonstrated a significant change in deuterium exchange profiles of the C-terminal regions between the extended and contracted R-body conformations. The C-termini of both Reb A and Reb B appear to be more protected from deuterium exchange in the extended low-pH ribbon than the contracted high-pH ribbon (Fig. 2.8 B). This increased protection at low pH implies an important relationship between pH-dependent re-structuring of the C-termini and the overall R-body conformation. Increased protection of the C-terminal region to deuterium exchange results from a more well-ordered peptide backbone in the C-terminal region at low pH, and this ordered backbone likely comes from a re-structuring to

α-helical secondary structure from a loose coil. It is also probable that the changes in structure of this C-terminal forms the dynamic lattice layer in the overall R-body ribbon.

To test the importance of the C-terminal regions of Reb A and Reb B in determining R-body conformation, we cloned R-body constructs with truncations of the C-termini of either Reb A, Reb B, or both Reb A and Reb B (referred to as the double truncation mutant). In comparison to the WT R-body, all C-terminal truncation mutants appeared to generate mutant complexes which appeared coiled similarly to the contracted R-body conformation but could not undergo the expected pH-responsive structural transition when visualized by negative stain electron microscopy (Fig. 2.11 A). The double C-termini truncation of Reb A and Reb B results in an overall coiled complex which appears more flexible than the WT pH 7 when observed by cryo-electron tomography. Moreover, comparison of sub-tomogram averages of the double truncation mutant and the WT pH 7 R-body show the presence of similar distinct lamina in the double truncation mutant (Fig. 2.11 B). These data demonstrate the essential role of the C-termini of Reb A and Reb B in both structure and function to the overall R-body complex.

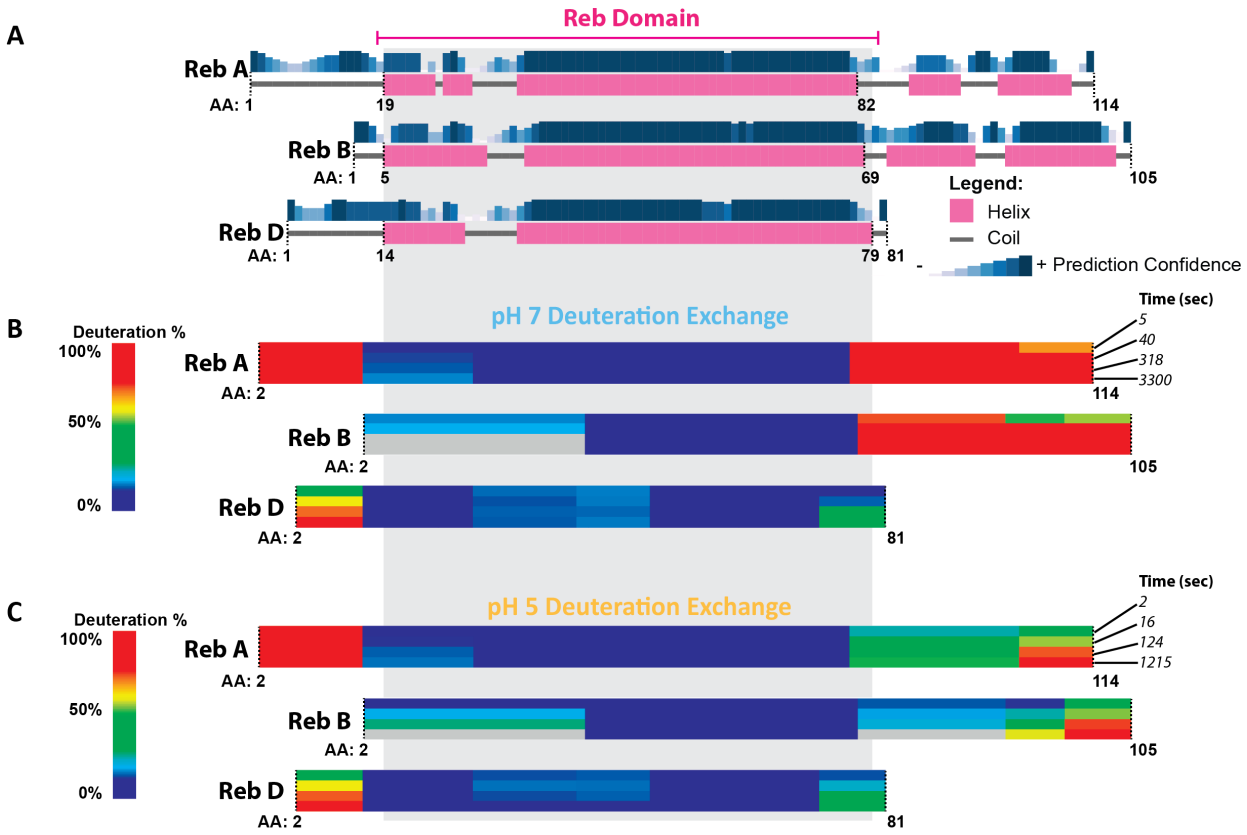

Figure 2.8: C-terminal regions of Reb A and Reb B proteins in the R-body ribbon

A) PsiPRED secondary structure predictions of Reb A, B, and D aligned by the shared reb domain. B) Time-resolved hydrogen-deuterium exchange profiles of Reb A, B and D at pH 7. C) Time-resolved hydrogen-deuterium exchange profiles of Reb A, B, and D at pH 5.

Figure 2.9: Secondary structure prediction of Reb A and Reb B

A) PsiPRED secondary structure prediction of Reb A. B) PsiPRED secondary structure prediction of Reb B.

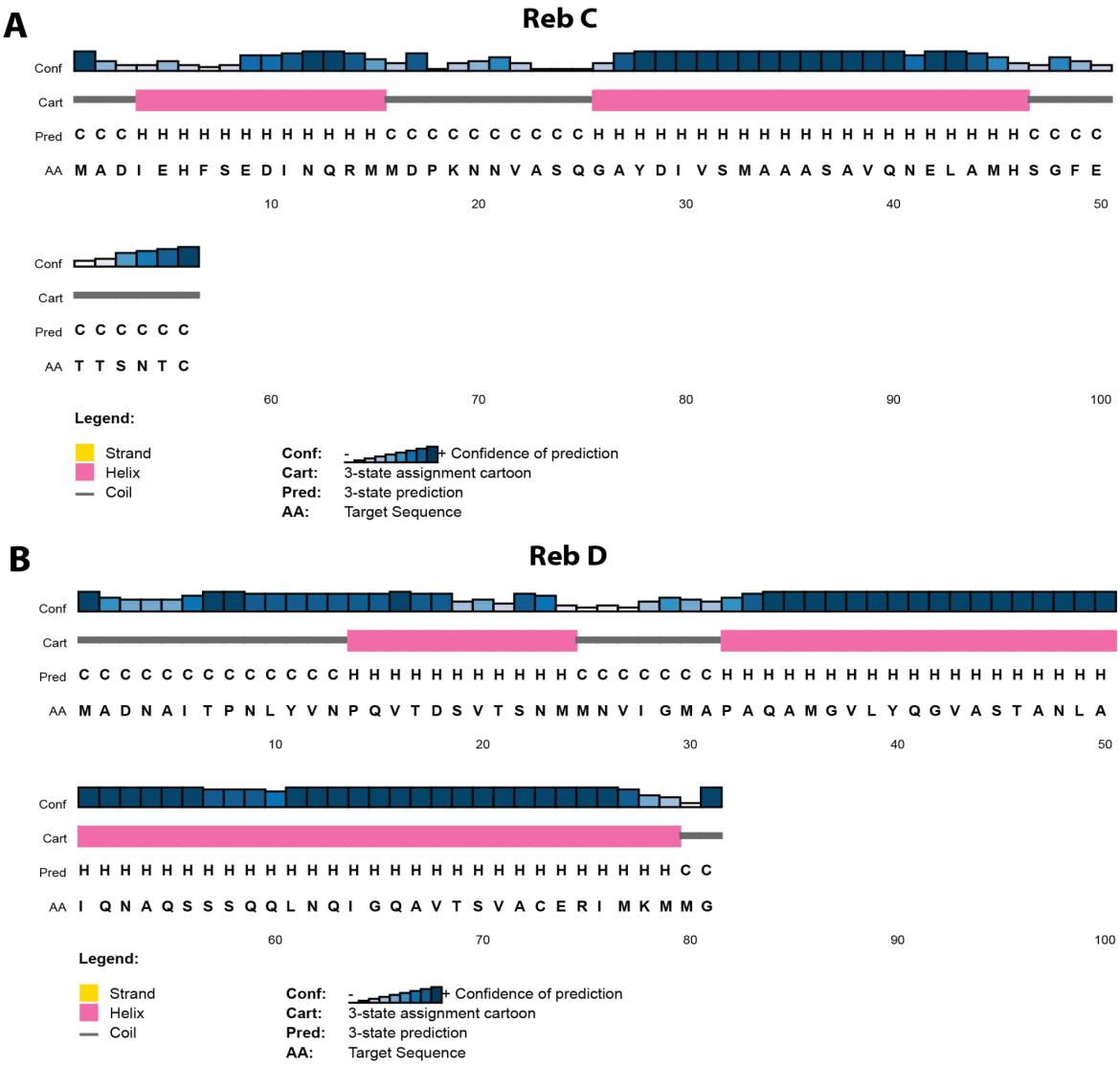

Figure 2.10: Secondary structure prediction of Reb C and Reb D

A) PsiPRED secondary structure prediction of Reb C. B) PsiPRED secondary structure prediction of Reb D.

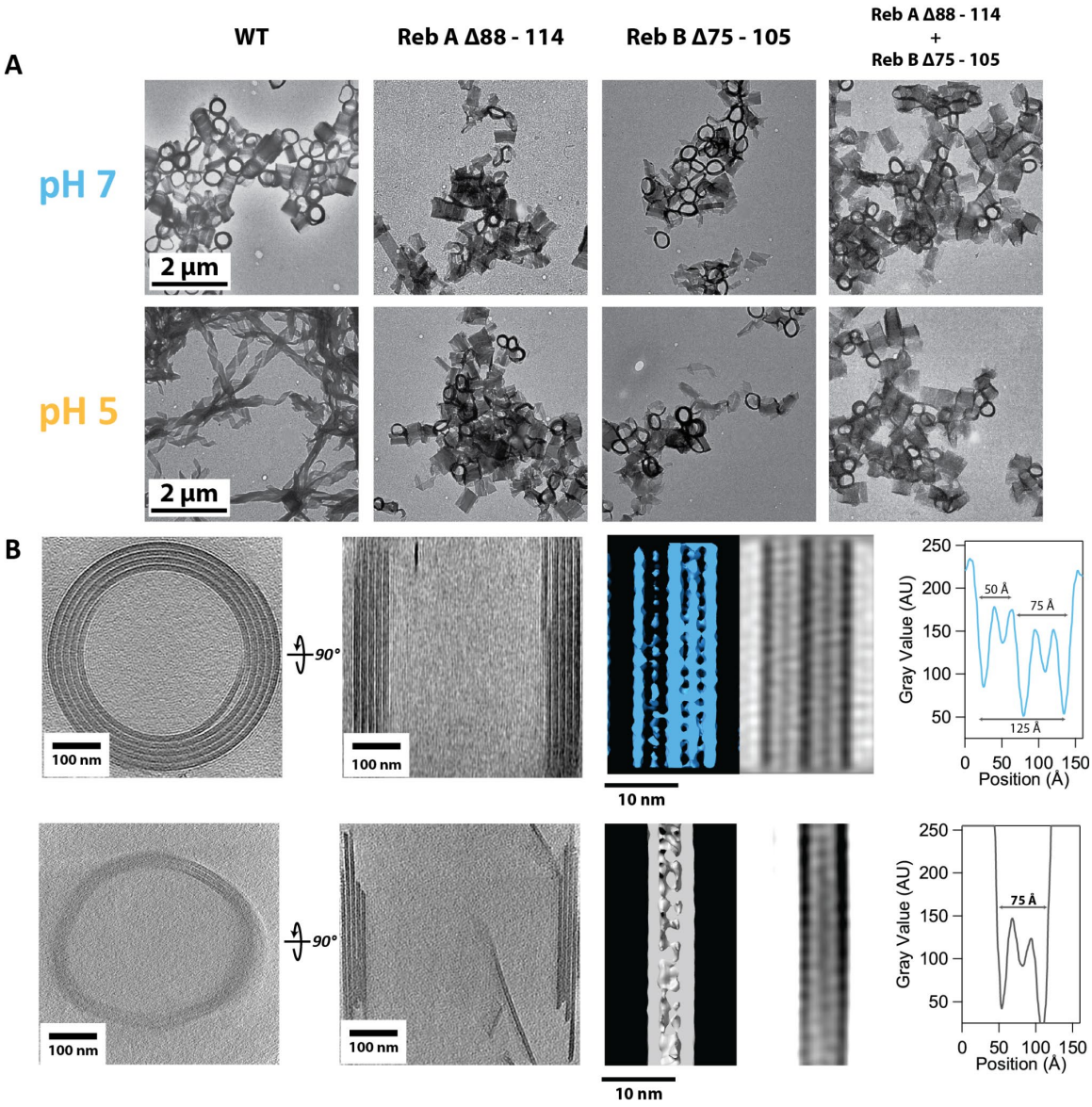

Figure 2.11: Truncation of Reb A and Reb B C-termini forms coiled R-body complexes which cannot undergo the expected structural transition in response to pH.

A) Negative stain micrographs of individual and combined C-terminal truncation constructs of Reb A and Reb B which demonstrate formation of coiled WT-like complexes lacking the pH-responsive conformational change. B) Tomogram of the WT at pH 7 (top) and combined Reb A and B C-terminal truncation construct (bottom) with the respective sub-tomogram averages low-pass filtered to 20Å (right).

3. Discussion

From the unit cell parameters of the ribbon lattice, we assume that each unit cell can only accommodate the width of a single alpha helical Reb A or Reb B arranged orthogonally to the lattice plane. Our experiments testing C-terminal truncations of Reb A and Reb B suggest that the proteins are arranged in parallel with the ordered N-terminal portion facing toward the outer radius and the dynamic C-terminal region facing toward the inner radius of the R-body complex. We find that the 20 Å difference in thickness of the R-body ribbon approximately corresponds to a transition in the 20 to 30 amino acid C-terminal region from loosely coiled or weakly alpha helical (assuming a mean rise of (1.5 + 3.5)/2 = ~2.5 Å per residue) to strongly alpha helical (with a rise of ~1.5 Å per residue). Given that both coiled and extended forms of the R-body ribbon share the same unit cell parameters, we assume the restructuring of the C-terminal region occurs around a stable lattice formed by the ordered N-terminal regions of Reb A and B. Thus, it appears that the overall R-body ribbon comprises at least two functional layers: an outer stable N-terminal lattice at all pH values and an inner C-terminal lattice which transitions from disordered at neutral pH to ordered at acidic pH.

The restructuring of the C-termini may promote new contacts between the portion of Reb A and Reb B facing the inner radius of the R-body. This has two important consequences. Firstly, the new contacts induce subtle changes in curvature between unit cells (on the order of 0.5°) which integrate over hundreds to thousands of unit cells to give the overall coiled or helical form. Secondly, the new contacts between unit cells on the inner surface of the R-body ribbon may integrate to form an overall tensile vector across the new inner lattice. Studies of helical

curvature in *Bauhinia* seed pods suggest that a differing radii of curvature can be induced in a bi-layered material depending on the relative angle between the tension vectors between the outer and inner layers (Forterre & Dumais, 2011). Thus, we propose that ordering of Reb A and Reb B C-termini at low pH into a lattice generates its own tension vector that is non-parallel with the static tension vector of the stable N-terminal lattice. These non-parallel tensions transition the R-body from its initial coiled state to the extended helical state. At neutral or basic pH, Reb A and Reb B C-termini are no longer ordered into a lattice and cannot generate significant tension to oppose the stable N-terminal lattice, which results in a transition from extended helix to coiled form in the overall R-body.

Our model highlights the critical role of nanoscale, pH-responsive restructuring in C-termini of Reb A and Reb B in driving the global, micron-scale changes in the full R-body complex. The essential role of the C-termini of Reb A and Reb B in R-body extensions and contractions was suggested by point-mutation experiments in (Polka & Silver, 2016). It was demonstrated that mutations within the C-terminal region of Reb A could shift the structural transition in response to pH in the mutant R-body complexes (Polka & Silver, 2016). Notably, mutation of Reb A G90A resulted in R-body complexes which could extend in more neutral pH buffered conditions (pH ~ 6.10) compared to WT. Substitution of glycine for alanine substitution would stabilize helical secondary structure in the C-terminal region and, consistent with our model predictions, promotes R-body extension at a less acidic pH threshold. On the other hand, introduction of a destabilizing Reb A S88P mutation resulted in R-body mutants with significantly impaired ability to extend and lyse *E. coli* compared to WT in acidic pH. This observation further reinforces our model's validity, as prevention of helical secondary structure in the Reb A C-

terminal would likely interfere with the ordering of the C-terminal lattice at low pH and thus prevent extension.

We can also apply our model to interpreting the kinetics of the pH-dependent transition speeds measured from DIC. For example, the lower maximal speed of extension can be explained by the presence of at least two different energy barriers. First, there is an enthalpic energy penalty to extension from needing to break the interactions between coils of the ribbon in the contracted form; it is likely that these interactions are dipole-dipole based given the systematic arrangement of N-termini and C-termini into two distinct layers in the R-body ribbon. Secondly, there is an entropic penalty to extension due to the ordering of the C-terminal layer from weakly alpha helical to strongly alpha helical secondary structure. By contrast, the contraction process should be strongly entropically favorable, and the coiled form is enthalpically stabilized by the inter-ribbon coil dipole-dipole interactions. Finally, the stable hysteresis observed at intermediate pH could be explained by the high degree of cooperativity expected between cross-linked unit cells in the ribbon array. Individual unit cells in either an extended or contracted array state would face energetic penalties for transitioning from their neighboring unit cells and would thus be influenced to remain in the same state as their neighboring unit cells without a sufficiently high pH change to drive the transition. An interesting question arises regarding the influence of changing temperature on an R-body's conformational state, assuming that pH and other buffer conditions are held constant. Our model predicts that increasing the temperature of the R-body would raise the entropy of the R-body, thus driving the disordered C-terminal state of Reb A and Reb B to promote the contracted conformation. Conversely, lowering the temperature of the R-body is predicted to lower the overall entropy of the R-body, which would lower the entropic

penalty of the ordering of the C-terminal layer and thus promote the extended conformation. Experiments which test the effect of temperature on the R-body conformation could be an interesting parameter of future directions as suggested in the next section of this differtation.

Our structural model of Type 51 R-bodies can assist understanding the mechanism of other types of R-bodies identified in many species of bacteria and pseudomonas. Type 51 R-bodies also have many characteristics which make them attractive model systems for protein engineering applications. For example, the extremely robust structure and consistent pH-controlled piston-like activity of R-bodies may make them an ideal system for the design of chemically responsive protein polymers. Finally, the role of R-bodies in cytotoxin delivery in nature presents R-bodies as a promising model system for controlled drug delivery systems (Li et al., 2017; Maleki et al., 2020).

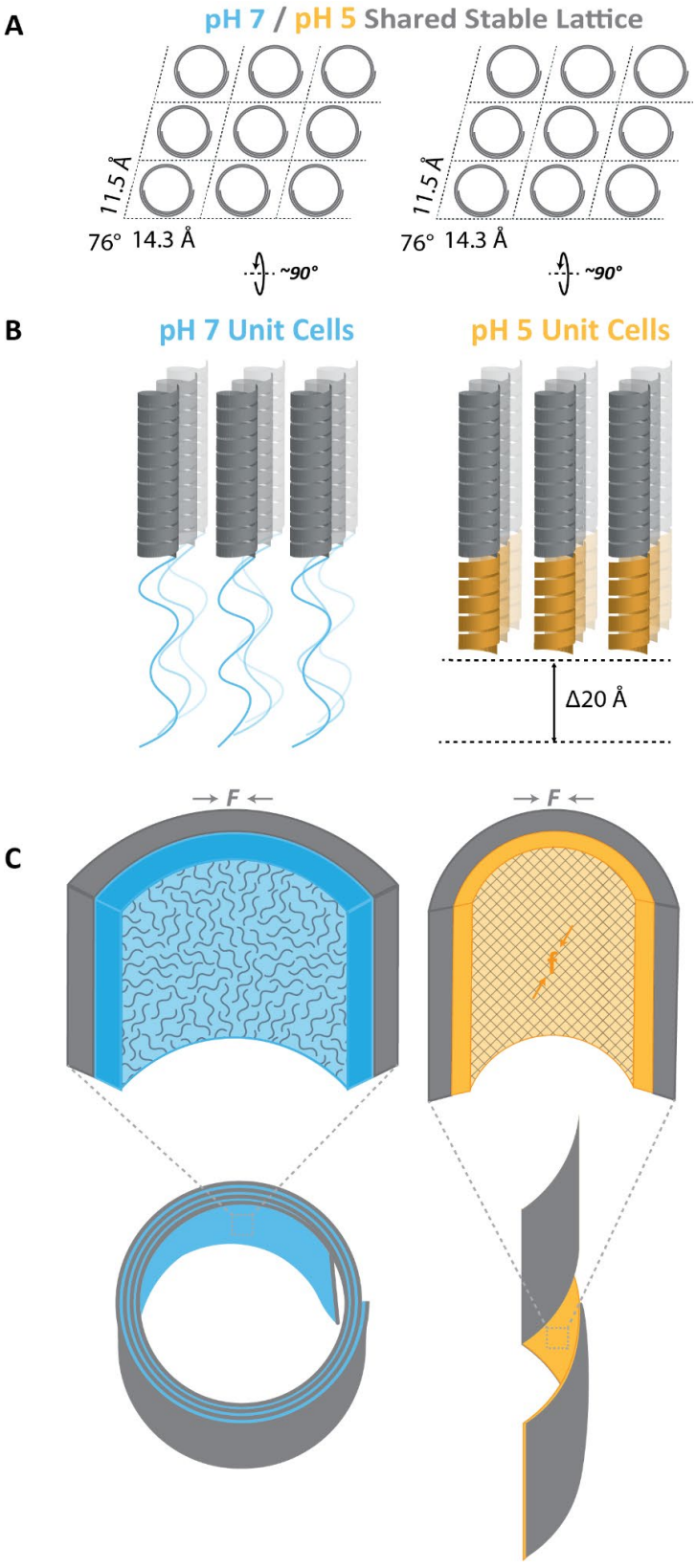
A
pH 7 / pH 5 Shared Stable Lattice
11.5 Å
76° 14.3 Å
~90°
11.5 Å
76° 14.3 Å
~90°
B
pH 7 Unit Cells
pH 5 Unit Cells
Δ20 Å
C
F
F

Figure 3.1: Mechanistic model of the R-body structural transition driven by restructuring of C-termini of Reb A and Reb B in response to changes in pH

A) A portion of the R-body ribbon remains as a stable lattice of cross-linked Reb A and Reb B irrespective of pH when viewed *en face*. B) The dynamic element of the R-body ribbon relies on the C-termini of Reb A and Reb B restructuring in response to pH, where the C-termini reorders from loose coils at neutral or basic pH to having definitive helical secondary structure at acid pH. C) Reb A and Reb B are arranged with the N-terminal region forming the stable lattice layer and the dynamic C-terminal region forming the inner layer. At low pH, the coordinated restructuring of the C-terminal regions of Reb A and Reb B C-termini results in the presence of a secondary lattice on the inner layer, which changes the balance of non-parallel tensile vectors within the R-body ribbon. The new tensile vectors result in subtle changes in local curvature between unit cells and dramatic changes in overall curvature of the R-body ribbon when unit-cell level changes are integrated over the entire length of the R-body complex. The change in both the magnitude and direction of the radius of curvature in the R-body ribbon thus drives the extension of the R-body complex from coiled to helical conformation.

4. Future Directions

The research presented in this thesis lays a structural foundation for describing the conformational change seen in R-bodies. During this project, it becomes clear that R-bodies have the potential to ignite new fields of exciting research. A few proposed future projects are suggested below regarding continuing the work done so far and improving our understanding of these unique protein machines. Laid out here are open questions which may be of interest in the immediate future studies of R-bodies.

Determination of conformational change propagation through an R-body ribbon by TIRF.

The propagation of conformational change through an R-body ribbon is not well characterized about the degree of stochasticity vs cooperativity; however, TIRF microscopy on sparsely labeled R-bodies has shown much promise. If conformational change is a stochastic process, we may expect to see changes in relative position between all pairs of fiducials along the length of the R-body which would arise from stochastic initiation of conformational change at random points in the R-body. On the other hand, if conformational change is a cooperative process, we should see conformational change initiate from specific positions on the R-body (most likely the ends) and propagate down the length of the R-body ribbon contour.

Preliminary TIRF results demonstrate a striking propagation of conformational change from one end of an extended R-body (Fig 4.1), further supporting the cooperativity hypothesis. This also implies that there is polarity to the R-body structure, potentially with one end of the structure

more sensitive to protonation and/or deprotonation than the other. However, many more conformational change events need to be captured by TIRF for statistical certainty. Data about conformational changes from speckle microscopy and transition kinetics from VE-DIC will provide the first mechanistic description of how individual R-bodies transition between coiled and extended states in response to different pH and buffering conditions. For example, it may be possible that the degree of stochasticity to cooperativity depends on the pH to which the R-bodies are exchanged: pH ranges which promote slow transitions may display a higher degree of cooperativity than more extreme pH values which favor rapid, multiple protonation or deprotonation events along the length of the R-body. These data will help to determine experimental parameters for measuring the force generating potential of R-bodies using optical traps.

Quantification of R-body force generation potential during pH induced conformational change.

R-bodies must generate considerable force to rupture membranes, but their actual force-generating capacity has never been measured. Initial attempts were made to measure R-body force generation by using the optical trap to hold on to a streptavidin functionalized polystyrene bead bound to a biotinylated R-body as the R-body undergoes a conformational change. The optical trap behaves as a Hookean spring, so any measured displacement of the bead from the beam of the optical trap can be used to calculate the forces generated by the contracting R-body. However, preliminary data show that a contracting R-body can repeatedly generate tensile forces over 140 pN when cycled between pH 5 and 7 (Fig 4.2). This currently exceeds the force-generating capacity of individual microtubules (Dogterom & Yurke, 1997) and actin filaments

(Footer et al., 2007) by more than an order of magnitude and indicates that R-bodies can maintain their force generating potential through multiple cycles of conformational change. Moreover, it is possible that the forces generated by R-body transitions might scale with pH in a manner like the transition velocities. If this is true, then laser trap forces might be sufficient to measurably slow or even stall the transitions that occur when an R-body is exchanged to a pH level near the hysteresis range. If a force-velocity relation can be measured near the hysteresis pH range, then a predicted maximum force can be estimated by extrapolation and might be validated using a different biophysical assay such as AFM, which can apply larger forces than laser trapping. In addition to force measurement, it may be possible to investigate the responsiveness of R-bodies to applied forces; we could exchange an extended R-body to different pH near hysteresis and apply ramping amounts of force with the optical trap to see if there is a threshold value of applied which force causes the extended R-body to transition. Such force response measurements could give a greater understanding of the energetics of protein folding during R-body structural transitions in response to different pH. With more force and kinetic measurements, we may understand how R-bodies harness chemical energy of protonation to generate mechanical work by creating a mathematical model which incorporates my structural and functional data (Fig 4.3).

High resolution R-body ribbon structures by 2D cryo-electron crystallography on R-body fragments.

A potential issue with the sub-tomogram averaging of the contracted R-body ribbon is the strongly preferred orientation of the coiled ultrastructure; the coiled form typically orients with the axis of extension upward. This results in lower quality structural resolution about the ribbon

lattice due to a “missing wedge” of information as one cannot tilt a tomographic sample to full 90° to retrieve all projection views. One approach may be to focus high-resolution structural work on R-body fragments. The work presented in this thesis research demonstrates that R-body fragments behave structurally in similar ways to complete R-body complexes. Thus. to supplement structural information about the ribbon lattice, 2D cryo-electron crystallography on R-body fragments may be a promising structural approach. Cryo-maps refined with 2D crystallographic data may prove of sufficient quality to begin building atomic models with supplemental information of backbone arrangement from solid-state NMR and AlphaFold. Such atomic models may help to figure out the stoichiometry of Reb A, B, and D within the R-body ribbon and the exact positions of the Reb elements in how they span the ribbon thickness.

Cell-free in vitro reconstitution of part or the entirety of R-body synthesis by combinatorial expression of Reb A, B, C, and D.

Future investigations of protein composition of the R-body ribbon may focus on the stoichiometry of incorporation of Reb A to Reb B and Reb D. It is not clear how Reb D is incorporated into the cross-linked lattice, and it is possible that Reb D is incorporated stochastically along the length of the R-body ribbon, and thus is not consistently detectable in the unit cell reflections in Fourier space. Moreover, it would be interesting to determine how the cross-linking of Reb A and Reb B influence the secondary structure of these Reb elements when incorporated into the R-body ribbon, as current secondary structure prediction only depict Reb A, B, and D as long, continuous helices in isolation. The chemical nature of Reb A and Reb B cross-linking is also yet unknown, and it is not clear what role Reb C plays in forming the overall R-body structure. Reb C may play a role in catalyzing iso-peptide cross-links between Reb A, B,

and D, or somehow help determine the width or contour length of the full R-body complexes, although it is also reasonable to assume that these physical dimensions must somehow limited by the cell volume of the recombinant E. coli which synthesize these R-bodies. Reproduction of the biochemistry of R-body synthesis in vitro (perhaps in a cell free system) may provide information regarding how Reb elements interact and what factors constrain the dimensions of R-body complexes.

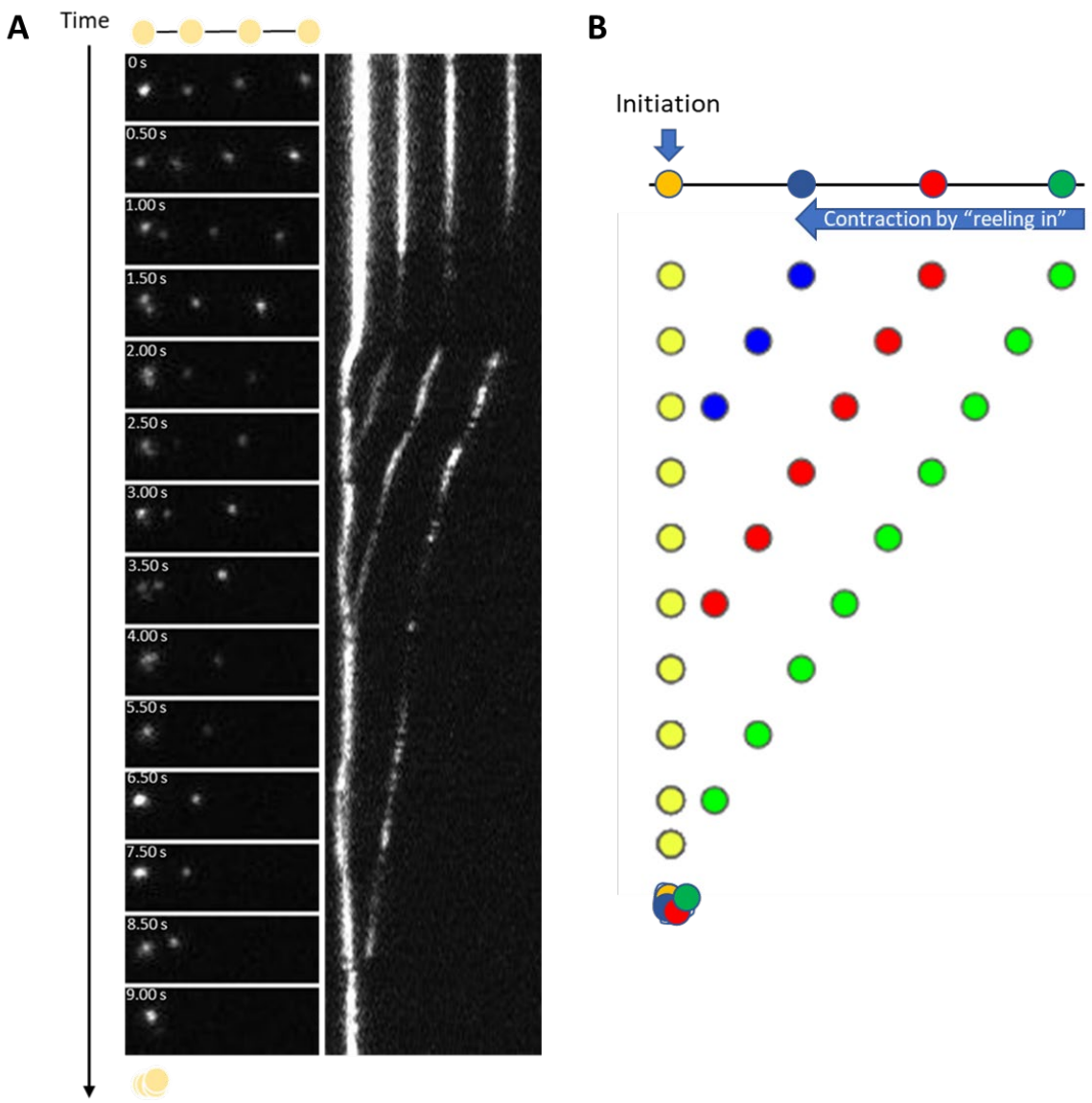

Figure 4.1: Fluorescence speckle TIRF demonstrates R-body transitions can have high cooperativity.

A) Time-lapse kymograph of the contraction of a sparsely labeled R-body. The R-body is biotinylated and incubated with low concentration of streptavidin functionalized fluorescent beads. B) The observation in (A) suggests a cooperative transition mechanism where the initiation of conformational change occurs at an end of the R-body with the rest of the R-body contracting toward the initiation point.

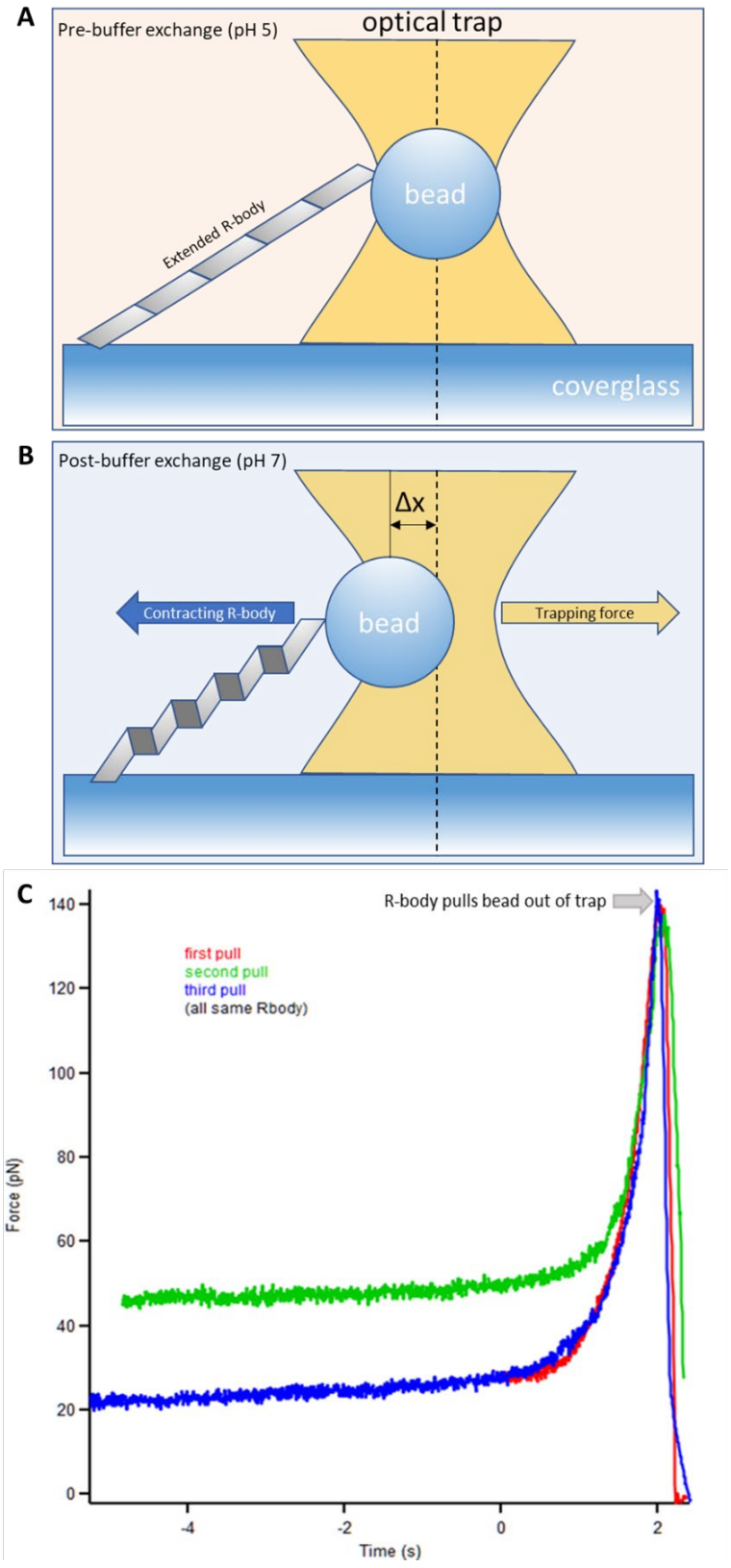
A
Pre-buffer exchange (pH 5)
optical trap
bead
Extended R-body
coverglass
B
Post-buffer exchange (pH 7)
Δx
Contracting R-body
bead
Trapping force
C
R-body pulls bead out of trap
first pull
second pull
third pull
(all same Rbody)
Force (pN)
Time (s)
140
120
100
80
60
40
20
0
-4
-2
0
2

Figure 4.2: R-bodies can reproducibly generate forces in excess of 140 pN when exposed to repeated pH cycles.

A, B) Schematic of optical trap experiment to measure forces on a contracting biotinylated R-body attached to a streptavidin polystyrene bead. C) Multiple measurements of force generation by a single R-body exposed to three pH cycles between pH 5 and 7. During this experiment, the R-body repeatedly pulled the bead out of the optical trap (on the stiffest setting) with no apparent resistance.

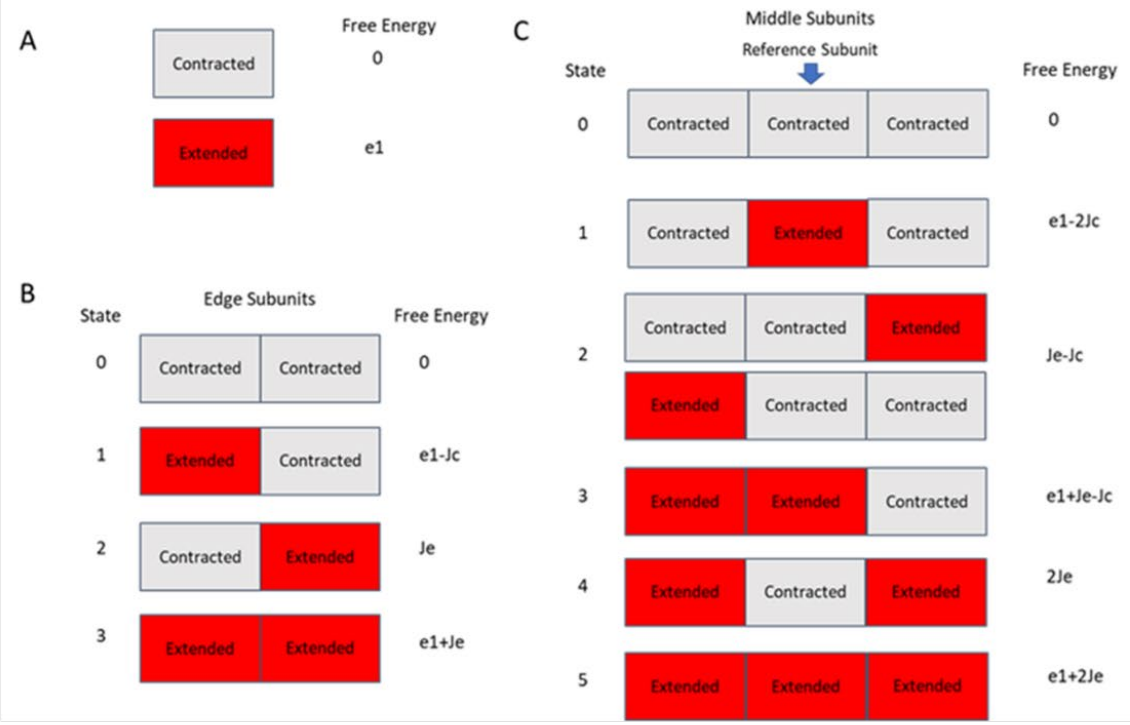
A
Contracted
Extended
Free Energy
0
e1
B
State
Edge Subunits
Free Energy
0
Contracted
Contracted
0
1
Extended
Contracted
e1-Jc
2
Contracted
Extended
Je
3
Extended
Extended
e1+Je
C
Middle Subunits
Reference Subunit
State
Free Energy
0
Contracted
Contracted
Contracted
0
1
Contracted
Extended
Contracted
e1-2Jc
2
Contracted
Contracted
Extended
Extended
Contracted
Contracted
Je-Jc
3
Extended
Extended
Contracted
e1+Je-Jc
4
Extended
Contracted
Extended
2Je
5
Extended
Extended
Extended
e1+2Je

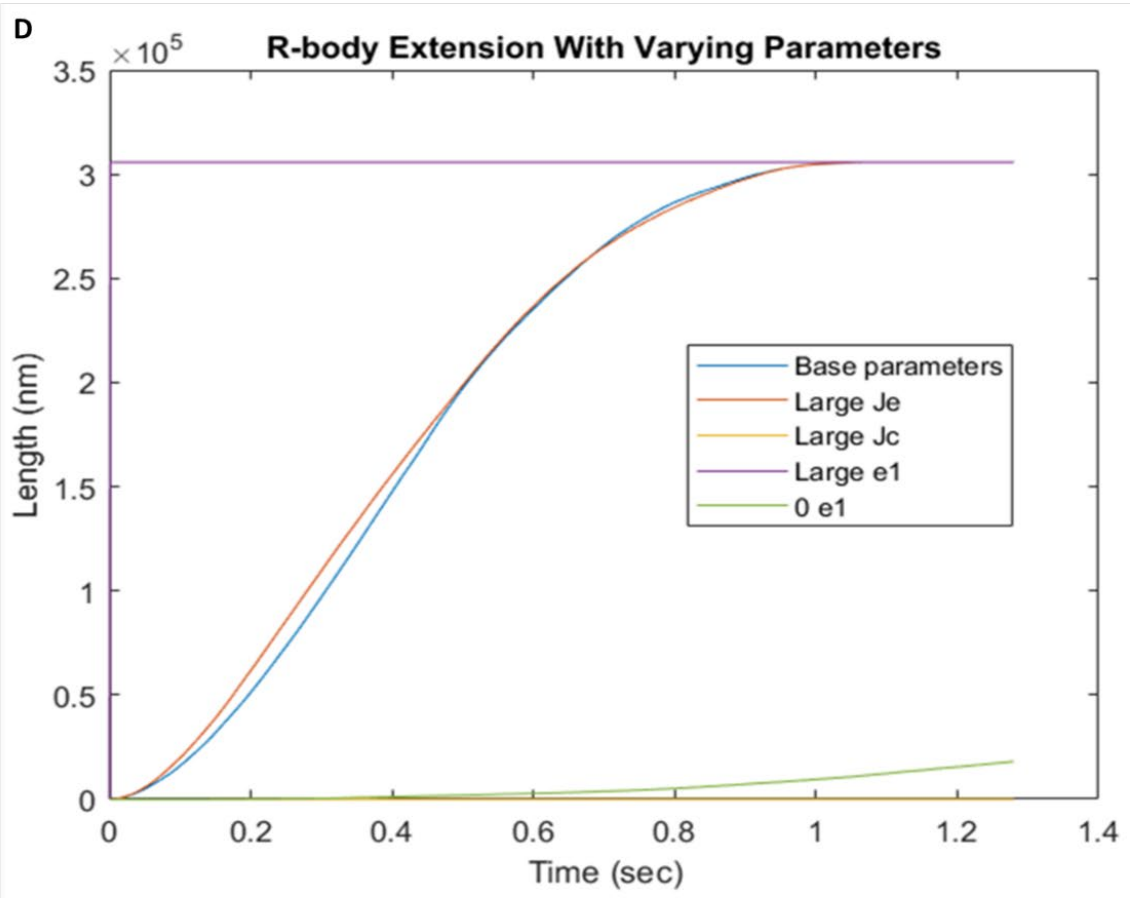
D
R-body Extension With Varying Parameters
×10^5
3.5
3
2.5
2
1.5
1
0.5
0
Length (nm)
0
0.2
0.4
0.6
0.8
1
1.2
1.4
Time (sec)
Base parameters
Large Je
Large Jc
Large e1
0 e1

Figure 4.3: A preliminary 1D mathematical model of R-body extension.

A) The assumption of a two-state system with ligand binding (i.e. protonation) tightly coupled to conformational change. B) Energy states detailing cooperative effects of neighboring subunits at the ends of the R-body. C) Energy states of subunits along the length of the R-body. D) Simulation of length vs. time changes in an extending R-body allowing for stochastic initiation of conformational change at any point in the R-body.

5. Methods

Cloning, expression, and purification of R-bodies

The purification method for R-bodies followed the method described in (Polka & Silver, 2016). Plasmids containing the wild-type Reb operon (A, B, C, D) under expression of T7 promoter in pETM11 were transformed into BL21DE3 *E. coli*. Cells were grown in Luria medium to OD 600 0.6 - 0.8 at 37 °C and induced with 1 mM IPTG. Expression proceeded for 18 h at 20 °C. To purify R bodies, cell pellets were flash-frozen in liquid nitrogen, then thawed. Cells were resuspended in 25 mM Tris pH 7.5, 100 mM NaCl, and 2 mM EDTA. Egg white lysozyme was added to a concentration of approximately 17 μg/mL, and cells were shaken at 200 RPM at 37 °C for 1 h. After this time, the buffer was adjusted to contain 10 mM MgCl2, 10 mM CaCl2, and approximately 15 μg/mL DNase from bovine pancreas. Cells were once again shaken at 200 RPM at 37 °C for 20 min. Next, the buffer was adjusted to contain 1% SDS. After manual mixing, cells were spun at 5000 x g for 20 min to pellet the R bodies. The R body pellet was then washed three times by resuspension in water, followed by spins, as above. R bodies were stored at −80 °C after flash-freezing in liquid nitrogen in the presence of 25 mM Tris pH 7.5, 100 mM KCl, and 15% glycerol. Q5 site directed mutagenesis was used to generate C-terminal truncation constructs of Reb A and Reb B from wild-type Reb A and Reb B sequences. The expression and purification of the C-terminal truncation constructs followed the same protocol as wild-type Reb operon plasmids.

Slide preparation for DIC microscopy

For experiments tracking R-body extensions and contractions by DIC microscopy, slides constructed with a channel ~1 cm wide were formed by bonding a plasma-cleaned glass coverslip to a clean glass slide using two parallel strips of double-stick tape. Purified R-bodies were diluted five to tenfold in pH 5 buffer (50 mM MES pH 5, 100 mM KCl) were loaded into the channel by pipetting 50 µL of sample onto one end of the channel and drawing the sample through the flow cell by wicking buffer with a wedge of blotting paper placed at the opposite end of the channel. The channel was then loaded with 50 µL of 1 mg/mL BSA in pH 5 buffer to passivate any unbound regions of the plasma-cleaned glass. 100 µL of pH 5 buffer was then flushed through the channel to clear any debris and excess protein. To induce contractions, R-bodies were exchanged from the initial pH 5 buffer to a more basic buffer of pH 6.25 - 8.25 by flowing 100 uL of buffer (10 mM MES pH 6.25 - 8.35, 100 mM KCl) through the flow channel using the pipette and blotting paper method described above. R-body extensions were similarly performed by exchanging the sample from an initial neutral buffer at pH 7 (10 mM MES pH 7.0, 100 mM KCl) to a more acidic buffer of pH 4.25 - 6.25 (10 mM MES pH 4.25 - 6.25, 100 mM KCl).

Tracking of individual R-body extension and contraction visualized by DIC

The full description of video enhanced differential interference contrast (VE-DIC) instrument set up is described in (Murray et al., 2022). Movies of R-body contractions and extensions were visualized by VE-DIC, with illumination by a mercury arc lamp (X-Cite 120) and accomplished through two standard Wollaston prisms and polarizers ((Walker et al., 1988)). The instrument was based around a Nikon inverted microscope (TE2000) with a Nikon 100×1.4 NA oil Plan Apo IR CFI objective. Movies from the DIC microscope were captured on a mounted video

camera and written to DVD. Movies were then copied from DVD, converted to AVI format using FFmpeg (Tomar, 2006), and imported to ImageJ (Abràmoff & Magalhães, 2004). The positions of individual R-bodies were tracked over time using MTrackJ (Meijering, n.d.). The length of each R-body was estimated over time by calculating the linear distance between the moving free tip in solution and the adhesion point on the coverslip glass. Speeds of extension and contraction were estimated by fitting a linear estimate to the middle of plots of R-body position vs. time. Speeds at each pH value were averaged and error bars shown with standard deviation.

Negative Stain Electron Microscopy

200 mesh copper grids were coated with Formvar and amorphous carbon. These grids were glow discharged for 1 min 30 s before applying R-body samples. For each condition visualized by negative stain electron microscopy, 10 - 25 µL of purified R-body sample was pelleted by centrifugation at 10,000 x g for 2 min in a tabletop centrifuge and resuspended in the appropriate buffer condition. The pellet and resuspension is repeated 1 to 2 times to ensure complete buffer exchange. 2 µL of the re-suspended R-body sample were applied to the glow discharged grid and incubated for 1 min. Excess sample was then wicked away with filter paper and stained with 2% uranyl formate. Grids were then washed sequentially with three drops of double deionized water and wicked with filter paper between each wash. After the final wash, the grids were dried for 30 minutes. Samples were imaged using an FEI Morgagni electron microscope operating at 100 kV and a Gatan Orius charge-coupled device (CCD) camera with the software package Digital Micrograph (v2.10.1282.0).

Cryo-electron Tomography

10 - 25 µL of purified R-body sample was pelleted by centrifugation at 10,000 x g for 2 min in a tabletop centrifuge and resuspended in either 10 mM MES pH 5, 100 mM KCl or 10 mM Tris-HCl pH 7, 100 mM KCl. 2 µL of the re-suspended R-body sample were applied to the glow discharged grid and incubated for 1 min were applied to glow-discharged C-flat 2/2 holey-carbon EM grids (Protochips), blotted, and plunge-frozen in liquid ethane using a FEI VitroBot apparatus at room temperature. Data collection was performed using an FEI Titan Krios transmission electron microscope operating at 300 kV (equipped with a Gatan image filter (GIF) and post-GIF Gatan K2 or K3 Summit direct electron detector) using SerialEM (Mastronarde, 2003). Tilt series were collected as dose-fractionated videos from -60° to +60° tilt angles in 2° increments using either a serial or dose-symmetric tilt scheme at 1.34 or 1.44 $e^-/Å^2$ at each tilt.

Tilt-series processing and Subtomogram Averaging

Videos were aligned, corrected for beam-induced motion, and organized into tilt series using Warp (Tegunov & Cramer, 2019). Tilt series were processed using the IMOD software package (Kremer et al., 1996), and initial CTF parameters were estimated with CTFPlotter. 2X binned tomograms were reconstructed to take measurements of ribbon thickness in ImageJ, and 10X binned tomograms were used to manually pick contours for subtomogram coordinates in 3dmod. The necessary IMOD files were processed using the Relion 4.0 subtomogram averaging processing pipeline (Zivanov et al., 2022).

Physical disruption of R-body complexes to generate fragments by high-pressure homogenization.

10 mL of purified R-body sample was centrifuged at 10,000 x g for 10 minutes and re-suspended in 10 mL of 10 mM MES pH 5, 50 mM KCl buffer. The sample was then recirculated on ice through an Avestin EmulsiFlex-c5 homogenizer (https://www.avestin.com/emulsiflex-c5.htm) using compressed air to maintain a pressure between 15 - 20 kPa for 20 minutes. At the end of homogenization, samples were collected, spun down and re-suspended in 10 mM Tris pH 7.0, 50 mM KCl buffer for flash freezing.

Lattice Images and Measurements

Movies were aligned and dose weighted using Appion frame alignment (myami/3.3) and micrographs were imported into Focus (https://lbem-focus.epfl.ch/about.php; https://www.sciencedirect.com/science/article/pii/S1047847717300515; v3.5.0). Micrographs were masked to a single RBody fragment and the 2DXtal module was used to calculate the lattice measurements from the Fast Fourier Transform of the masked micrograph. Masked micrographs were then exported from Focus and imported into Fiji (v2.1.0/1.53c), where a Fast Fourier Transform was applied to the micrograph, followed by Gaussian filtering and contrast adjustment for figure generation.

Image processing in ImageJ

R-body thicknesses were measured by projecting through 20 slices of tomogram binned to (~5 Angstrom per pixel) in 3dmod. Line-plots were generated in ImageJ by integrating over a

rectangular box on each projection image. Half-max x-values taken midway between the peak of Fresnel fringes and corresponding troughs. Thickness is estimated by taking the difference between the positions at each half-max value. Other parameters were measured directly in ImageJ using line-tool.

Atomic force microscopy

R-body stock solution was diluted 10 times with MES buffer (pH 5 or 7) and 100 mM KCl. 5-10 µl diluted R-body solution was deposited onto freshly cleaved mica (Ted Pella, CA) and incubated for 10 min. Then the surface was rinsed by MES buffer (pH 5 or 7) with 100 mM KCl three times. The samples were imaged with Cypher-ES AFM (Asylum Research, CA) using amplitude modulation mode and SNL-10-A probe (Bruker, CA). The in-situ AFM experiments with the buffer exchange were done with a home-built perfusion system developed at Molecular Foundry. The data processing was done with SPIP software (Image Metrology, Denmark).

Reb A, B, and D secondary structure prediction with PSIPRED

Amino acid sequences of Reb A, B, and D (UNIPROT Accession: Q57297, Q46365, and Q57342 respectively) were submitted in FASTA format to PSIPRED 4.0 server (McGuffin et al., 2000).

Hydrogen-Deuterium Exchange

For each time point, 10 uL of R-body sample were incubated at room temperature in either neutral deuterated buffer (85% D2O, pH/pD 6.7) for 5; 40; 318; or 3300 s or in acidic deuterated

buffer (85% D2O, pH/pD 5.3) for 2; 16; 124; or 1215 s. Samples were subsequently mixed with an equal volume of ice-cold quench buffer (4 M urea, 200 mM tris(2-chlorethyl) phosphate (TCEP), 0.2% formic acid) to a final pH of 2.5 then immediately frozen in liquid nitrogen for storage at −80 °C until analysis. Online digestion was performed with a pepsin column prepared using the protocol described by Wang et al. (L. Wang et al., 2002) and analyzed by LC-MS utilizing a Thermo Orbittrap Elite mass spectrometer as described previously utilizing a 15 min gradient and a home-made HDX cold box that maintains the pepsin digestion at 5°C and the LC plumbing at 0°C (Watson et al., 2021). Pepsin digestion efficiency was confirmed using the protocol described by Vorauer et al. (Vorauer et al., 2021). Peptides were identified using Byonic (Version 3.8, Protein Metrics Inc.) with deamidation at N and Q, oxidation at C, M, W, and Y, and N-terminal cyclization at E and Q variable modifications selected. Deuterium uptake analysis was performed with HD-Examiner (Version 2.5, Sierra Analytics). The percentage exchange was normalized to undeuterated and fully deuterated reference samples. Internal exchange reporters described by Murphree et al. were included in each reaction to ensure that conditions were consistent throughout all the labeling reactions (Murphree et al., 2020).

6. References

Abràmoff, M. D., & Magalhães, P. J. (2004). Image processing with ImageJ. *Biophotonics*. https://dspace.library.uu.nl/handle/1874/204900

Dogterom, M., & Yurke, B. (1997). Measurement of the force-velocity relation for growing microtubules. *Science*, *278*(5339), 856–860.

Footer, M. J., Kerssemakers, J. W. J., Theriot, J. A., & Dogterom, M. (2007). Direct measurement of force generation by actin filament polymerization using an optical trap. *Proceedings of the National Academy of Sciences of the United States of America*, *104*(7), 2181–2186.

Forterre, Y., & Dumais, J. (2011). Generating Helices in Nature. *Science*, *333*(6050), 1715–1716.

Jeblick, J., & Kusch, J. (2005). Sequence, Transcription Activity, and Evolutionary Origin of the R-BodyCoding Plasmid pKAP298 from the Intracellular Parasitic BacteriumCaedibacter taeniospiralis. *Journal of Molecular Evolution*, *60*(2), 164–173.

Kanabrocki, J. A., Quackenbush, R. L., & Pond, F. R. (1986). Organization and expression of genetic determinants for synthesis and assembly of type 51 R bodies. *Journal of Bacteriology*, *168*(1), 40–48.

Kremer, J. R., Mastronarde, D. N., & McIntosh, J. R. (1996). Computer visualization of three-dimensional image data using IMOD. *Journal of Structural Biology*, *116*(1), 71–76.

Li, W., Liu, D., Zhang, H., Correia, A., Mäkilä, E., Salonen, J., Hirvonen, J., & Santos, H. A. (2017). Microfluidic assembly of a nano-in-micro dual drug delivery platform composed of halloysite nanotubes and a pH-responsive polymer for colon cancer therapy. *Acta Biomaterialia*, *48*, 238–246.

Maleki, R., Afrouzi, H. H., Hosseini, M., Toghraie, D., Piranfar, A., & Rostami, S. (2020). pH-sensitive loading/releasing of doxorubicin using single-walled carbon nanotube and multi-walled carbon nanotube: A molecular dynamics study. *Computer Methods and Programs in Biomedicine*, *186*, 105210.

Mastronarde, D. N. (2003). SerialEM: A Program for Automated Tilt Series Acquisition on Tecnai Microscopes Using Prediction of Specimen Position. *Microscopy and Microanalysis: The Official Journal of Microscopy Society of America, Microbeam Analysis Society, Microscopical Society of Canada*, *9*(S02), 1182–1183.

McGuffin, L. J., Bryson, K., & Jones, D. T. (2000). The PSIPRED protein structure prediction server. *Bioinformatics* , *16*(4), 404–405.

Meijering, E. (n.d.). MTrackJ: A Java program for manual object tracking. *Rotterdam: University Medical Center Rotterdam*.

Murphree, T. A., Vorauer, C., Brzoska, M., & Guttman, M. (2020). Imidazolium Compounds as Internal Exchange Reporters for Hydrogen/Deuterium Exchange by Mass Spectrometry. *Analytical Chemistry*, *92*(14), 9830–9837.

Murray, L. E., Kim, H., Rice, L. M., & Asbury, C. L. (2022). Catching the Conformational Wave: Measuring the Working Strokes of Protofilaments as They Curl Outward from Disassembling Microtubule Tips. *Methods in Molecular Biology* , *2478*, 653–676.

Polka, J. K., & Silver, P. A. (2016). A Tunable Protein Piston That Breaks Membranes to Release Encapsulated Cargo. *ACS Synthetic Biology*, *5*(4), 303–311.

Pond, F. R., Gibson, I., Lalucat, J., & Quackenbush, R. L. (1989). R-body-producing bacteria. *Microbiological Reviews*, *53*(1), 25–67.

Preer, J. R., Jr. (1975). The hereditary symbionts of Paramecium aurelia. *Symposia of the Society for Experimental Biology*, *29*, 125–144.

Preer, J. R., Jr, Preer, L. B., & Jurand, A. (1974). Kappa and other endosymbionts in Paramecium aurelia. *Bacteriological Reviews*, *38*(2), 113–163.

Quackenbush, R. L. (1983). Plasmids from bacterial endosymbionts of hump-killer paramecia. *Plasmid*, *9*(3), 298–306.

Quackenbush, R. L., & Burbach, J. A. (1983). Cloning and expression of DNA sequences associated with the killer trait of Paramecium tetraurelia stock 47. *Proceedings of the National Academy of Sciences of the United States of America*, *80*(1), 250–254.

Schrallhammer, M., Galati, S., Altenbuchner, J., Schweikert, M., Görtz, H.-D., & Petroni, G. (2012). Tracing the role of R-bodies in the killer trait: absence of toxicity of R-body producing recombinant E. coli on paramecia. *European Journal of Protistology*, *48*(4), 290–296.

Sonneborn, T. M. (1938). Mating Types in Paramecium Aurelia: Diverse Conditions for Mating in Different Stocks; Occurrence, Number and Interrelations of the Types. *Proceedings of the American Philosophical Society*, *79*(3), 411–434.

Tegunov, D., & Cramer, P. (2019). Real-time cryo-electron microscopy data preprocessing with Warp. *Nature Methods*, *16*(11), 1146–1152.

Tomar, S. (2006). Converting video formats with FFmpeg. *Linux Journal*, *2006*(146), 10.

Vorauer, C., Wrigley, M. S., Rincon Pabon, J. P., Watson, M. J., Mundorff, C. C., Weis, D. D., & Guttman, M. (2021). Rapid Assessment of Pepsin Column Activity for Reliable HDX-MS Studies. *Journal of the American Society for Mass Spectrometry*, *32*(9), 2386–2390.

Walker, R. A., O'Brien, E. T., Pryer, N. K., Soboeiro, M. F., Voter, W. A., Erickson, H. P., & Salmon, E. D. (1988). Dynamic instability of individual microtubules analyzed by video light microscopy: rate constants and transition frequencies. *The Journal of Cell Biology*, *107*(4), 1437–1448.

Wang, B., Lin, Y.-C., Vasquez-Rifo, A., Jo, J., Price-Whelan, A., McDonald, S. T., Brown, L. M., Sieben, C., & Dietrich, L. E. P. (2021). Pseudomonas aeruginosa PA14 produces R-bodies, extendable protein polymers with roles in host colonization and virulence. *Nature Communications*, *12*(1), 4613.

Wang, L., Li, Y., Chen, X., Chen, J., Gautam, S. C., Xu, Y., & Chopp, M. (2002). MCP-1, MIP-1, IL-8 and Ischemic Cerebral Tissue Enhance Human Bone Marrow Stromal Cell Migration in Interface Culture. *Hematology* , *7*(2), 113–117.

Watson, M. J., Harkewicz, R., Hodge, E. A., Vorauer, C., Palmer, J., Lee, K. K., & Guttman, M. (2021). Simple Platform for Automating Decoupled LC–MS Analysis of Hydrogen/Deuterium Exchange Samples. *Journal of the American Society for Mass Spectrometry*, *32*(2), 597–600.

Zivanov, J., Otón, J., Ke, Z., von Kügelgen, A., Pyle, E., Qu, K., Morado, D., Castaño-Díez, D., Zanetti, G., Bharat, T. A. M., Briggs, J. A. G., & Scheres, S. H. W. (2022). A Bayesian approach to single-particle electron cryo-tomography in RELION-4.0. *eLife*, *11*. https://doi.org/10.7554/eLife.83724